Deep reinforcement learning for the control of conjugate heat transfer with application to workpiece cooling

Elie Hachem, Hassan Ghraieb, Jonathan Viquerat, Aurélien Larcher, P. Meliga

Deep reinforcement learning for the control of conjugate heat transfer with application to workpiece cooling

A Preprint

Elie Hachem
MINES Paristech , PSL - Research University, CEMEF

H. Ghraieb
MINES Paristech , PSL - Research University, CEMEF

J. Viquerat*
MINES Paristech , PSL - Research University, CEMEF
jonathan.viquerat@mines-paristech.fr

A. Larcher
MINES Paristech , PSL - Research University, CEMEF

P. Meliga
MINES Paristech , PSL - Research University, CEMEF

November 30, 2020

Abstract

This research gauges the ability of deep reinforcement learning (DRL) techniques to assist the control of conjugate heat transfer systems. It uses a novel, "degenerate" version of the proximal policy optimization (PPO) algorithm to train a neural network in optimizing said system only once per learning episode, and an in-house stabilized finite elements environment combining variational multiscale (VMS) modeling of the governing equations, immerse volume method, and multi-component anisotropic mesh adaptation to compute the numerical reward fed to the neural network. Several test cases of natural and forced convection are used as testbed for developing the methodology, that proves successful to alleviate the heat transfer enhancement related to the onset of convection in a two-dimensional, differentially heated square cavity, and to improve the homogeneity of temperature across the surface of two and three-dimensional hot workpieces under impingement cooling. Beyond adding value to the shallow literature on this subject, these findings establish the potential of single-step PPO for reliable black-box optimization of computational fluid dynamics (CFD) systems, and pave the way for future progress in the optimal control of conjugate heat transfer using this new class of methods.

Keywords Deep Reinforcement Learning; Artificial Neural Networks; Conjugate heat transfer; Computational fluid dynamics; Thermal control

*Corresponding author

1 Introduction

Thermal control, defined as the ability to finesse the thermal properties of a volume of fluid (and of the solid objects inside) into a certain desired state, is a field of tremendous societal and economical importance. For instance, heat/cool exchangers are used in a broad range of industrial applications to regulate process temperatures by heat or cool transfer between fluid media, which in turn ensures that machinery, chemicals, water, gas, and other substances remain within safe operating conditions. Green building engineering is another field relying on such ability to manage indoor thermal conditions (temperature, humidity) under substantial variations of the ambient conditions to provide high-quality living and working environments. In many manufacturing processes, thermal conditioning is also intended to improve the final mechanical (e.g., hardness, toughness, resistance), electrical, or optical properties of the product, the general picture being that high temperature gradients are useful to speed up the process but generally harm the quality of the outcome because of heat transfer inhomogeneities caused by the increased convection by the fluid particles. All such problems fall under the purview of this line of study.

Numerous strategies have been implemented to control fluid mechanical systems (including conjugate heat transfer systems combining thermal conduction in the solid and convective transfer in the fluid), either open-loop with passive appendices (e.g., end plate, splitter plate, small secondary cylinder, or flexible tail), or open-loop with actuating devices (e.g., plasma actuation, boundary temperatures, steady or unsteady base bleeding, rotation) or closed-loop (e.g. via transverse motion, perturbations of the thermal boundary layer, blowing/suction, rotation, all relying on an appropriate sensing of flow variables). Nonetheless, many of the proposed strategies are trial and error, and therefore require extensive and costly experimental or numerical campaigns. This has motivated the development of analytical methods and numerical algorithms for the optimal control of Navier–Stokes systems [1, 2, 3], and the maturing of mathematical methods in flow control and discrete concepts for PDE constrained optimization. Applications to the heat equation [4] and the coupled Navier–Stokes and heat equations [5, 6, 7, 8] have also been considered, including fresh developments meant to alter the linear amplification of flow disturbances [9], but the general picture remains that the optimal control of conducting, convecting fluids has not been extensively studied.

The premise of this research is that the related task of selecting an optimal subset of control parameters can alternatively be assisted by machine learning algorithms. Indeed, the introduction of the back-propagation algorithm [10] has progressively turned Artificial Neural Networks (ANN) into a family of versatile non-parametric tools that can be trained to hierarchically extract informative features from data and to provide qualitative and quantitative modeling predictions. Together with the increased affordability of high performance computational hardware, this has allowed leveraging the ever-increasing volume of data generated for research and engineering purposes into novel insight and actionable information, which in turn has entirely transformed scientific disciplines, such as robotics [11, 12] or image analysis [13]. Owing to the ability of neural networks to handle stiff, large-scale nonlinear problems [14], machine learning algorithms have also been making rapid inroads in fluid mechanics, as a mean to solve the Navier–Stokes equations [15] or to predict closure terms in turbulence models [16]; see also Ref. [17] for an overview of the current developments and opportunities.

Neural networks can also be used to solve decision-making problems, which is the purpose of Deep Reinforcement Learning (DRL, where the *deep* terminology generally weighs on the sizable depth of the network), an advanced branch of machine learning. Simply put, a neural network trains in finding out which actions or succession of actions maximize a numerical reward signal, with the possibility for a given action to affect not only the immediate but also the future rewards. Successful applications of DRL range from AlphaGo, the well-known ANN that defeated the top-level human player at the game of Go [18] to the real-word deployment of legged robots [19], to breakthroughs in computer vision (e.g., filtering, or extracting image features) [20] and optimal control problems [21, 22]. Despite the many achievements, DRL remains surprisingly sparsely used in fluid mechanics, with a limited amount of literature barely scratching the surface of the performance improvements to be delivered in low-Reynolds-number flow control [23, 24, 25] and shape optimization [26]. The literature on thermal control is even more sparse, with only Ref. [27] addressing the control of natural convection dominated heat transfer (this is a recent effort similar to the present work, conducted in the same time frame, that we became aware of during the redaction of this manuscript), plus a few other publications dealing with energy efficiency in civil engineering from low-dimensional thermodynamic models basically unrelated to the equations of fluid dynamics [28, 29].

This research assesses the feasibility of using proximal policy optimization (PPO [22]) for control and optimization purposes of conjugate heat transfer systems, as governed by the coupled Navier–Stokes and heat equations. The objective here is to keep shaping the capabilities of the method (PPO is still a relatively newcomer that has quickly emerged as the go-to DRL algorithm due to its data efficiency, simplicity of implementation and reliable performance) and to narrow the gap between DRL and advanced numerical methods for multiscale, multi-physics computational fluid dynamics (CFD). We investigate more specifically the "degenerate" single-step PPO algorithm introduced in [26], in which the neural network gets only one attempt per learning episode at finding the optimal. Several problems of conjugate heat transfer in two and three dimensions are used as testbed to push forward the development of this novel approach, whose high potential as a reliable black-box optimizer for CFD problems (where only the final configuration is of interest) has been recently assessed for aerodynamic applications [30]. To the best of the authors knowledge, this constitutes the first attempt to achieve DRL-based control of *forced* convection (with [27] being the first attempt to achieve DRL control of *natural* convection, to give credit where it is due).

The organization is as follows: section 2 outlines the main features of the finite element CFD environment used to compute the numerical reward fed to the neural network, that combines variational multiscale (VMS) modeling of the governing equations, immerse volume method, and multi-component anisotropic mesh adaptation. The baseline principles and assumptions of DRL and PPO are presented in section 3, together with the specifics of the single-step PPO algorithm. Section 4 revisits the natural convection case of [27] for the purpose of validation and assessment part of the method capabilities. In section 5, DRL is used to control conjugate heat transfer in a model setup of two-dimensional workpiece cooling by impingement of a fluid. An extension to three-dimensional workpieces is proposed in section 6.

2 Computational fluid dynamics

The focus of this research is on conjugate heat transfer and laminar, incompressible fluid flow problems in two and three-dimensions, for which the conservation of mass, momentum and energy is described by the nonlinear, coupled Navier–Stokes and heat equations

$$\nabla \cdot \boldsymbol{u} = 0\,, \tag{1}$$

$$\rho(\partial_t \boldsymbol{u} + \boldsymbol{u} \cdot \nabla \boldsymbol{u}) = \nabla \cdot (-p\mathbf{I} + 2\mu\boldsymbol{\varepsilon}(\boldsymbol{u})) + \boldsymbol{\psi}\,, \tag{2}$$

$$\rho c_p(\partial_t T + \boldsymbol{u} \cdot \nabla T) = \nabla \cdot (\lambda \nabla T) + \chi\,, \tag{3}$$

where $\boldsymbol{u}$ is the velocity field, p is the pressure, T is the temperature, $\boldsymbol{\varepsilon}(\boldsymbol{u}) = (\nabla \boldsymbol{u} + \nabla \boldsymbol{u}^T)/2$ is the rate of deformation tensor, $\boldsymbol{\psi}$ and χ are source terms (modeling, e.g., buoyancy or radiative heat transfer), and we assume here constant fluid density ρ, dynamic viscosity μ, thermal conductivity λ, and specific heat c_p.

2.1 The immersed volume method

The numerical modeling of conjugate heat transfer mostly depends upon a heat transfer coefficient to ensure that the proper amount of heat is exchanged at the fluid/solid interface via thermal boundary conditions. Computing said coefficient is no small task (as it requires solving an inverse problem to assimilate experimental data, which in turn requires relevant experimental data to be available), and is generally acknowledged to be a limiting issue for practical applications where one must vary, e.g., the shape, number and position of the solid, or the fluid and/or solid material properties. We thus rather use here the immerse volume method (IVM) to combine both the fluid and solid phases into a single fluid with variable material properties. Simply put, we solve equations formally identical to (1)-(3) on a unique computational domain Ω, but with variable density, dynamic viscosity, conductivity, and specific heat, which removes the need for a heat transfer coefficient since the amount of heat exchanged at the interface then proceeds solely from the individual material properties on either side of it. In order to ensure numerical accuracy, such an approach must combine three key ingredients, that are briefly reviewed in the next paragraphs: an interface capturing method, anisotropic mesh adaptation to achieve a high-fidelity description of said interface, and relevant mixing laws to describe the properties of the composite fluid. One point worth being mentioned is that the interface here is static, although the same numerical framework can be used to dynamically track moving interfaces, and thus to encompass the effect of solid displacements. This is because the solid is fixed once an action has been taken by the PPO agent, although not fixed over the course of optimization, as the solid position can very well be the quantity subjected to optimization, as illustrated in section 5.3.4.

- Level set method: the level set approach is used to localize the fluid/solid interface by the zero iso-value of a smooth function. In practice, a signed distance function ϕ is used to localize the interface and initialize the material properties on both either side of it, with the convention that $\phi > 0$ (res. $\phi < 0$) in the fluid (resp. the solid).

- Anisotropic mesh adaptation: the interface may intersect arbitrarily the mesh elements if it is not aligned with the element edges, in which case discontinuous material properties across the interface can yield oscillations of the numerical solutions. We thus use the anisotropic mesh adaptation technique presented in [31] to ensure that the material properties are distributed as accurately and smoothly as possible over the smallest possible thickness around the interface. This is done computing modified distances from a symmetric positive defined tensor (the metric) whose eigenvectors define preferential directions along which mesh sizes can be prescribed from the related eigenvalues. The metric used here is isotropic far from the interface, with mesh size set equal to h_∞ in all directions, but anisotropic near the interface, with mesh size equal to $h_\perp$ in the direction normal to the interface, and to h_∞ in the other directions, which can be written for an intended thickness δ as

$$\boldsymbol{M} = K(\phi)\boldsymbol{n}\otimes\boldsymbol{n} + \frac{1}{h_\infty}\boldsymbol{I} \qquad \text{with} \qquad K(\phi) = \begin{cases} 0 & \text{if } |\phi| \geq \delta/2\,, \\ \dfrac{1}{h_\perp^2} - \dfrac{1}{h_\infty^2} & \text{if } |\phi| < \delta/2\,, \end{cases} \tag{4}$$

where $\boldsymbol{n} = \nabla\phi/||\nabla\phi||$ is the unit normal to the fluid/solid interface computed from the level set gradient. A posteriori anisotropic error estimator is then used to minimize the interpolation error under the constraint of a fixed number of edges in the mesh. A unique metric can be built from multi-component error vectors [31, 32, 33, 34], which is especially relevant for conjugate heat transfer optimization, as it allows each learning episode to use an equally accurate mesh adapted from the velocity vector and magnitude, the temperature field, and the level set.

- Mixing laws: the composite density, dynamic viscosity and specific heat featured in equations (1)-(3) are computed by linear interpolation of the fluid and solid values, for instance the composite density is

$$\rho = \rho_f H_\epsilon(\phi) + \rho_s(1 - H_\epsilon(\phi))\,, \tag{5}$$

where H_ϵ is the smoothed Heaviside function defined as

$$H_\epsilon(\phi) = \begin{cases} 0 & \text{if } \phi < -\epsilon\,, \\ \dfrac{1}{2}(1 + \dfrac{\phi}{\epsilon} + \dfrac{1}{\pi}\sin(\pi\dfrac{\phi}{\epsilon})) & \text{if } |\phi| \leq \epsilon\,, \\ 1 & \text{if } \phi > \epsilon\,, \end{cases} \tag{6}$$

and ϵ is a regularization parameter proportional to the mesh size in the normal direction to the interface, set here to $\epsilon = 2h_\perp$. Doing so for the thermal conductivity would however lead to inaccurate results [35], hence the inverse of the thermal conductivity is linearly interpolated according to

$$\frac{1}{\lambda} = \frac{1}{\lambda_f}H_\epsilon(\phi) + \frac{1}{\lambda_s}(1 - H_\epsilon(\phi))\,, \tag{7}$$

to ensure conversation of the heat flux.

2.2 Variational multiscale approach (VMS)

In the context of finite element methods (that remain widely used to simulate engineering CFD systems due to their ability to handle complex geometries), direct numerical simulation (DNS) solves the weak form of (1)-(3), obtained by integrating by parts the pressure, viscous and conductive terms, to give

$$(\rho(\partial_t\boldsymbol{u} + \boldsymbol{u}\cdot\nabla\boldsymbol{u})\,,\,\boldsymbol{w}) + (2\mu\boldsymbol{\varepsilon}(\boldsymbol{u})\,,\,\boldsymbol{\varepsilon}(\boldsymbol{w})) - (p\,,\,\nabla\cdot\boldsymbol{w}) + (\nabla\cdot\boldsymbol{u}\,,\,q) = (\boldsymbol{\psi}\,,\,\boldsymbol{w})\,, \tag{8}$$

$$(\rho c_p(\partial_t T + \boldsymbol{u}\cdot\nabla T)\,,\,s) + (\lambda\nabla T\,,\,\nabla s) = (\chi\,,\,s)\,, \tag{9}$$

where $(\,,\,)$ is the L^2 inner product on the computational domain, $\boldsymbol{w}$, q and s are relevant test functions for the velocity, pressure and temperature variables, and all fluid properties are those mixed with the smoothed Heaviside function defined in (6).

We use here the variational multiscale (VMS) approach [36, 37, 38] to solve a stabilized formulation of (8)-(9), which allows circumventing the Babuska—Brezzi condition (that otherwise imposes that different interpolation orders be used to discretize the velocity and pressure variables, while we use here simple continuous piecewise linear P_1 elements for all variables) and prevents numerical instabilities in convection regimes at high Reynolds numbers. We shall not go into the extensive details about the derivation of the stabilized formulations, for which the reader is referred to [39, 40]. Suffice it to say here that the flow quantities are split into coarse and fine scale components, that correspond to different levels of resolution. The fine scales are solved in an approximate manner to allow modeling their effect into the large-scale equations, which gives rise to additional terms in the right-hand side of (8)-(9), and yields the following weak forms for the large scale

$$\begin{aligned}(\rho(\partial_t \boldsymbol{u} + \boldsymbol{u}\cdot\nabla\boldsymbol{u})\,,\,\boldsymbol{w}) + (2\mu\boldsymbol{\varepsilon}(\boldsymbol{u})\,,\,\boldsymbol{\varepsilon}(\boldsymbol{w})) - (p\,,\,\nabla\cdot\boldsymbol{w}) + (\nabla\cdot\boldsymbol{u}\,,\,q) &= (\boldsymbol{\psi}\,,\,\boldsymbol{w}) \\ + \sum_{K\in\mathcal{T}_h}\left[(\tau_1\mathcal{R}_M\,,\,\boldsymbol{u}\cdot\nabla\boldsymbol{w})_K + (\tau_1\mathcal{R}_M\,,\,\nabla q)_K + (\tau_2\mathcal{R}_C\,,\,\nabla\cdot\boldsymbol{w})_K\right], &\qquad (10)\\ (\rho c_p(\partial_t T + \boldsymbol{u}\cdot\nabla T)\,,\,s) + (\lambda\nabla T\,,\,\nabla s) &= (\chi\,,\,s) \\ + \sum_{K\in\mathcal{T}_h}\left[(\tau_3\mathcal{R}_T\,,\,\boldsymbol{u}\cdot\nabla s)_K + (\tau_4\mathcal{R}_T\,,\,\boldsymbol{u}_\parallel\cdot\nabla s)_K\right], &\qquad (11)\end{aligned}$$

where $(\,,\,)_K$ is the inner product on element K, and the $\mathcal{R}$ terms are residuals for the governing equations defined by

$$-\mathcal{R}_C = \nabla\cdot\boldsymbol{u}\,,\quad -\mathcal{R}_M = \rho(\partial_t\boldsymbol{u} + \boldsymbol{u}\cdot\nabla\boldsymbol{u}) + \nabla p - \boldsymbol{\psi}\quad -\mathcal{R}_T = \rho c_p(\partial_t T + \boldsymbol{u}\cdot\nabla T) - \chi\,, \qquad (12)$$

In (10), $\tau_{1,2}$ are ad-hoc mesh-dependent stabilization parameters defined in [41, 42]. In (11), $\boldsymbol{u}_\parallel$ is the projection of the velocity along the direction of the temperature gradient, and $\tau_{3,4}$ are mesh-independent stabilization parameters acting both in the direction of the solution and of its gradient, that proceed from the stabilization of the ubiquitous convection-diffusion-reaction equation [43, 44], whose definition is given in [45, 46].

The governing equations are solved sequentially, i.e., we solve first (10), then use the resulting fluid velocity to solve (11). All linear systems are preconditioned with a block Jacobi method supplemented by an incomplete LU factorization, and solved with the GMRES algorithm, with tolerance threshold set to 10^{-6} for the Navier–Stokes equations, and 10^{-5} for the heat equation. The time derivatives, source and VMS stabilization terms are approximated explicitly with the forward Euler scheme. The viscous, pressure and divergence terms of the Navier–Stokes equations are integrated implicitly with the backward Euler scheme. The convection term is discretized semi-implicitly using the first-order backward Newton–Gregory formula, which yields

$$\begin{aligned}(\rho(\frac{\boldsymbol{u}^{i+1}-\boldsymbol{u}^i}{\Delta t} + \boldsymbol{u}^i\cdot\nabla\boldsymbol{u}^{i+1})\,,\,\boldsymbol{w}) + (2\mu\boldsymbol{\varepsilon}(\boldsymbol{u}^{i+1})\,,\,\boldsymbol{\varepsilon}(\boldsymbol{w})) - (p^{i+1}\,,\,\nabla\cdot\boldsymbol{w}) + (\nabla\cdot\boldsymbol{u}^{i+1}\,,\,q) &= (\boldsymbol{\psi}^i\,,\,\boldsymbol{w}) \\ + \sum_{K\in\mathcal{T}_h}\left[(\tau_1^i\mathcal{R}_M^{i+1}\,,\,\boldsymbol{u}^i\cdot\nabla\boldsymbol{w})_K + (\tau_1^i\mathcal{R}_M^{i+1}\,,\,\nabla q)_K + (\tau_2^i\mathcal{R}_C^{i+1}\,,\,\nabla\cdot\boldsymbol{w})_K\right], &\qquad (13)\end{aligned}$$

with residuals

$$-\mathcal{R}_C^{i+1} = \nabla\cdot\boldsymbol{u}^{i+1}\,,\quad -\mathcal{R}_M^{i+1} = \rho(\frac{\boldsymbol{u}^{i+1}-\boldsymbol{u}^i}{\Delta t} + \boldsymbol{u}^i\cdot\nabla\boldsymbol{u}^{i+1}) + \nabla p^{i+1} - \boldsymbol{\psi}^i\,, \qquad (14)$$

where the i superscript refers to the solution at time $t_i = i\Delta t$. The convection and conduction terms of the heat equation are integrated implicitly with the backward Euler scheme, to give

$$\begin{aligned}(\rho c_p(\frac{T^{i+1}-T^i}{\Delta t} + \boldsymbol{u}^{i+1}\cdot\nabla T^{i+1})\,,\,s) + (\lambda\nabla T^{i+1}\,,\,\nabla s) &= (\chi^i\,,\,s) \\ + \sum_{K\in\mathcal{T}_h}\left[(\tau_3^i\mathcal{R}_T^{i+1}\,,\,\boldsymbol{u}^{i+1}\cdot\nabla s)_K + (\tau_4^i\mathcal{R}_T^{i+1}\,,\,\boldsymbol{u}_\parallel^{i+1}\cdot\nabla s)_K\right], &\qquad (15)\end{aligned}$$

with residual

$$-\mathcal{R}_T^{i+1} = \rho c_p(\frac{T^{i+1}-T^i}{\Delta t} + \boldsymbol{u}^{i+1}\cdot\nabla T^{i+1}) - \chi^i\,. \qquad (16)$$

We solve (13)-(15) with an in-house VMS solver whose accuracy and reliability with respect to the intended application has been assessed in a series of previous papers; see especially [47, 42] for a detailed presentation of the mathematical formulation relevant to the IVM of a rigid body in an incompressible fluid and [40, 48] for an application to conjugate heat transfer analysis.

3 Deep reinforcement learning and proximal policy optimization

3.1 Neural networks

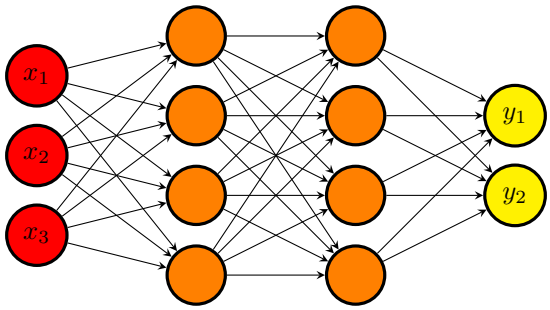

Figure 1: Fully connected neural network with two hidden layers, modeling a mapping from $\mathbb{R}^3$ to $\mathbb{R}^2$.

A neural network (NN) is a collection of artificial neurons, i.e., connected computational units that can be trained to arbitrarily well approximate the mapping function between input and output spaces. Each connection provides the output of a neuron as an input to another neuron. Each neuron performs a weighted sum of its inputs, to assign significance to the inputs with regard to the task the algorithm is trying to learn. It then adds a bias to better represent the part of the output that is actually independent of the input. Finally, it feeds an activation function that determines whether and to what extent the computed value should affect the outcome. As sketched in figure 1, a fully connected network is generally organized into layers, with the neurons of one layer being connected solely to those of the immediately preceding and following layers. The layer that receives the external data is the input layer, the layer that produces the outcome is the output layer, and in between them are zero or more hidden layers.

The design of an efficient neural network requires a proper optimization of the weights and biases, together with a relevant nonlinear activation function. The abundant literature available on this topic points to a relevant network architecture (e.g., type of network, depth, width of each layer), finely tuned hyper parameters (i.e., parameters whose value cannot be estimated from data, e.g., optimizer, learning rate, batch size) and a sufficiently large amount of data to learn from as being the key ingredients for success; see, e.g., Ref. [49] and the references therein.

3.2 Deep reinforcement learning

Deep reinforcement learning (DRL) is an advanced branch of machine learning in which deep neural networks train in solving sequential decision-making problems. It is a natural extension of reinforcement learning (RL), in which an agent (the neural network) is taught how to behave in an environment by taking actions and by receiving feedback from it under the form of a reward (to measure how good or bad the taken action was) and information (to gauge how the action has affected the environment). This can be formulated as a Markov Decision Process, for which a typical execution goes as follows (see also figure 2):

- assume the environment is in state $s_t \in \mathcal{S}$ at iteration t, where $\mathcal{S}$ is a set of states,
- the agent uses w_t, an observation of the current environment state (and possibly a partial subset of s_t) to take action $a_t \in \mathcal{A}$, where $\mathcal{A}$ is a set of actions,
- the environment reacts to the action and transitions from s_t to state $s_{t+1} \in \mathcal{S}$,
- the agent is fed with a reward $r_t \in \mathcal{R}$, where $\mathcal{R}$ is a set of rewards, and a new observation w_{t+1},

This repeats until some termination state is reached, the succession of states and actions defining a trajectory $\tau = \big(s_0, a_0, s_1, a_1, ...\big)$. In any given state, the objective of the agent is to determine the action maximizing its cumulative reward over an episode, i.e., over one instance of the scenario in which the agent takes actions.

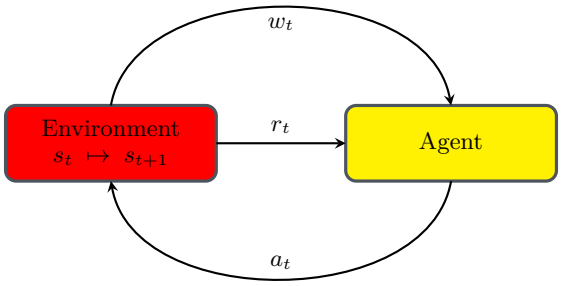

Figure 2: RL agent and its interactions with its environment.

Most often, the quantity of interest is the discounted cumulative reward along a trajectory defined as

$$R(\tau) = \sum_{t=0}^{T} \gamma^t r_t \,, \tag{17}$$

where T is the horizon of the trajectory, and $\gamma \in [0, 1]$ is a discount factor that weighs the relative importance of present and future rewards (the agent being short-sighted in the limit where $\gamma \to 0$, since it then cares solely about the first reward, and far-sighted in the limit where $\gamma \to 1$, since it then cares equally about all rewards).

There exist two main types of RL algorithms, namely model-based methods, in which the agent tries to build a model of how the environment works to make predictions about what the next state and reward will be before taking any action, and model-free methods, in which the agent conversely interacts with the environment without trying to understand it, and are prominent in the DRL community. Another important distinction to be made within model-free algorithms is that between value-based methods, in which the agent learns to predict the future reward of taking an action when provided a given state, then selects the maximum action based on these estimates, and policy-based methods, in which it optimizes the expected reward of a decision policy mapping states to actions. Many of the most successful algorithms in DRL (including proximal policy optimization, whose assessment for flow control and optimization purposes is the primary motivation for this research) proceed from policy gradient methods, in which gradient ascent is used to optimize a parameterized policy with respect to the expected return, as further explained in the next section. The reader interested in a more thorough introduction to the zoology of RL methods (together with their respective pros and cons) is referred to Ref. [50].

3.3 From policy methods to Proximal policy optimization

This section intended for the non-specialist reader briefly reviews the basic principles and assumptions of policy gradient methods, together with the various steps taken for improvement.

- Policy methods. A policy method maximizes the expected discounted cumulative reward of a decision policy mapping states to actions. It resorts not to a value function, but to a probability distribution over actions given states, that fully defines the behavior of the agent. Since policies are most often stochastic, the following notations are introduced:

- $\pi(s, a)$ is the probability of taking action a in state s under policy π,
- $Q^\pi(s, a)$ is the expected value of the return of the policy after taking action a in state s (also termed state-action value function or Q-function)

$$Q^\pi(s, a) = \mathbb{E}_\pi\big[R(\tau)|s, a\big] \,, \tag{18}$$

- $V^\pi(s)$ is the expected value of the return of the policy in state s (also termed value function or V-function)

$$V^\pi(s) = \mathbb{E}_\pi\big[R(\tau)|s\big]\,. \tag{19}$$

The V and Q functions are therefore such that

$$V^\pi(s) = \sum_a \pi(s,a) Q^\pi(s,a)\,, \tag{20}$$

so $V^\pi(s)$ can also be understood as the probability-weighted average of discounted cumulated rewards over all possible actions in state s.

- Policy gradient methods. A policy gradient method aims at optimizing a parametrized policy π_θ, where θ denotes the free parameters whose value can be learnt from data (as opposed to the hyper parameters). In practice, one defines an objective function based on the expected discounted cumulative reward

$$J(\theta) = \mathbb{E}_{\tau\sim\pi_\theta}\big[R(\tau)\big]\,, \tag{21}$$

and seeks the parameterization θ^* maximizing $J(\theta)$, hence such that

$$\theta^* = \arg\max_\theta \mathbb{E}_{\tau\sim\pi_\theta}\big[R(\tau)\big]\,, \tag{22}$$

which can be done on paper by plugging an estimator of the policy gradient $\nabla_\theta J(\theta)$ into a gradient ascent algorithm. This is no small task as one is looking for the gradient with respect to the policy parameters, in a context where the effects of policy changes on the state distribution are unknown (since modifying the policy will most likely modify the set of visited states, which will in turn affect performance in some indefinite manner). The most commonly used estimator, derived in [50] using the log-probability trick, reads

$$\nabla_\theta J(\theta) = \mathbb{E}_{\tau\sim\pi_\theta}\left[\sum_{t=0}^{T} \nabla_\theta \log\left(\pi_\theta(s_t,a_t)\right) R(\tau)\right] \sim \mathbb{E}_{\tau\sim\pi_\theta}\left[\sum_{t=0}^{T} \nabla_\theta \log\left(\pi_\theta(s_t,a_t)\right) A^\pi(s,a)\right]\,, \tag{23}$$

where the rightmost term is a convenient approximation relying on the advantage function

$$A^\pi(s,a) = Q^\pi(s,a) - V^\pi(s)\,, \tag{24}$$

that measures the improvement (if $A > 0$, otherwise the lack thereof) associated with taking action a in state s compared to taking the average over all possible actions. This is because the value function does not depend on θ, so taking it off changes neither the expected value, nor the gradient, but it does reduce the variance, and speeds up the training. Furthermore, when the policy π_θ is represented by a neural network (in which case θ simply denotes the network weights and biases to be optimized), the focus is rather on the policy loss defined as

$$L(\theta) = \mathbb{E}_{\tau\sim\pi_\theta}\left[\sum_{t=0}^{T} \log\left(\pi_\theta(a_t|s_t)\right) A^\pi(s,a)\right]\,, \tag{25}$$

whose gradient is equal to the (approximated) policy gradient (23) (since the gradient operator acts only on the log-policy term, not on the advantage) and is computed with respect to each weight and bias by the chain rule, one layer at the time, using the back-propagation algorithm [10].

- Trust regions. The performance of policy gradient methods is hurt by the high sensitivity to the learning rate, i.e., the size of the step to be taken in the gradient direction. Indeed, small learning rates are detrimental to learning, but large learning rates can lead to a performance collapse if the agent falls off the cliff and restarts from a poorly performing state with a locally bad policy. This is all the more harmful as the learning rate cannot be tuned locally, meaning that an above average learning rate will speed up learning in some regions of the parameter space where the policy loss is relatively flat, but will possibly trigger an exploding policy update in other regions exhibiting sharper variations. One way to ensure continuous improvement is by imposing a trust region constraint to limit the difference between the current and updated policies, which can be done by determining first a maximum step size relevant

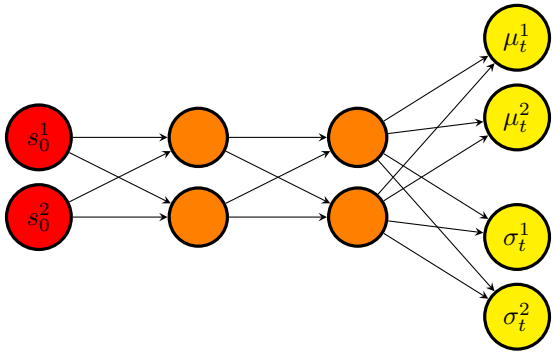

Figure 3: Agent network example used to map states to policy. The input state $\boldsymbol{s_0}$, here of size 2, is mapped to a mean $\boldsymbol{\mu}$ and a standard deviation $\boldsymbol{\sigma}$ vectors, each of size 2. All activation functions are ReLu, except for that of the last layer, which are linear for the μ output, and softplus for the σ output. Orthogonal weights initialization is used throughout the network.

for exploration, then by locating the optimal point within this trust region. We will not dwell on the intricate details of the many algorithms developed to solve such trust region optimization problems, e.g., natural policy gradient (NPG [51]), or trust region policy optimization (TRPO [52]). Suffice it to say that they use the minorize-maximization algorithm to maximize iteratively a surrogate policy loss (i.e. a lower bound approximating locally the actual loss at the current policy), but are difficult to implement and can be computationally expensive, as they rely on an estimate of the second-order gradient of the policy log probability.

- Proximal policy optimization. Proximal policy optimization (PPO) is another approach with simple and effective heuristics, that uses a probability ratio between the two policies to maximize improvement without the risk of performance collapse [22]. The focus here is on the PPO-clip algorithm[2], that optimizes the surrogate loss

$$L(\theta) = \mathbb{E}_{(s,a)\sim\pi_\theta}\left[\min\left(\frac{\pi_\theta(a|s)}{\pi_{\theta_{old}}(a|s)}A^{\pi_\theta}(s,a), g(\epsilon, A^{\pi_\theta}(s,a))\right)\right], \tag{26}$$

where

$$g(\epsilon, A) = \begin{cases}(1+\epsilon)A & A \geq 0\,,\\ (1-\epsilon)A & A < 0\,,\end{cases} \tag{27}$$

and $\epsilon \in [0.1, 0.3]$ is the clipping range, a small hyper parameter defining how far away the new policy is allowed to go from the old. In practice, a state-action pair yielding a positive advantage will cause $\pi_\theta(a|s)$ to increase for the action to become more likely. By doing so, if it increases in a way such that $\pi_\theta(a|s) > (1+\epsilon)\pi_{\theta_{old}}(a|s)$, the min kicks in (26) and its argument hits a ceiling of $(1+\epsilon)A^{\pi_\theta}(s,a)$. Conversely, a state-action pair yielding a negative advantage will cause $\pi_\theta(a|s)$ to decrease for the action to become less likely. If it increases in a way such that $\pi_\theta(a|s) < (1-\epsilon)\pi_{\theta_{old}}(a|s)$, the max kicks in and its argument hits a ceiling of $(1-\epsilon)A^{\pi_\theta}(s,a)$. In neither case does the new policy has any incentive to step too far away from the current policy, which ensures that both policies will behave similarly.

The strengths of the approach lie in the fact that the clipped surrogate itself is cheap to compute, and that it needs only an estimate of the first-order gradient of the policy log probability (like policy gradient methods). Refinements have been proposed recently, for instance the Trust region PPO (TRGPPO) that adaptively adjusts the clipping range within the trust region [53], but classic PPO is generally acknowledged to be one of the most successful DRL method, combining ease of implementation and tuning, together with state-of-the-art performance across a wide range of challenging tasks.

[2]There is also a PPO-Penalty variant which uses a penalization on the average Kullback–Leibler divergence between the current and new policies, but PPO-clip performs better in practice.

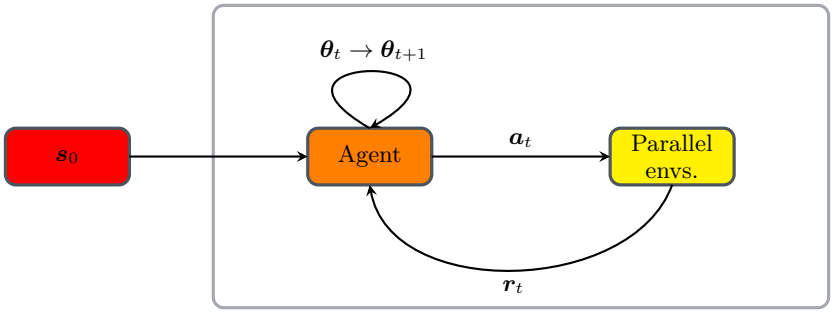

Figure 4: Action loop for single-step PPO. At each episode, the input state $\boldsymbol{s}_0$ is provided to the agent, which in turn provides n actions to n parallel environments. The latter return n rewards, that evaluate the quality of each action taken. Once all the rewards are collected, an update of the agent parameters is made using the PPO loss (26).

3.4 Single-step PPO

We now come to the single-step PPO method proposed in [26], a "degenerate" version of PPO in which the agent and the environment get to exchange only one single triplet (s, a, r) per learning episode. This represents a significant difference with respect to classic Markov-based methods. and amounts to view the agent as a parameterized mapping $f_{\boldsymbol{\theta}}$ from state to action.

As sketched in figure 3, the agent is consistently fed with the same input state $\boldsymbol{s}_0$ (usually a vector of zeros), and outputs a policy π that can be represented by mean and standard deviation vectors (denoted by $\boldsymbol{\mu}$ and $\boldsymbol{\sigma}$, respectively) whose size matches the dimension of the action required by the environment. The optimization loop is as follows: first, the agent implements a random mapping $f_{\boldsymbol{\theta}_0}$ from $\boldsymbol{s}_0$ to an initial policy determined by the initialization of the network parameters $\boldsymbol{\theta}_0$. At each iteration, a population of actions $\boldsymbol{a}_t = f_{\boldsymbol{\theta}_t}(s_0)$ is drawn from the current policy, the reward associated to each set of action is computed and the agent is returned incentives (through the rewards) to update the free parameters in a way such that the next population of actions $\boldsymbol{a_{t+1}} \sim f_{\boldsymbol{\theta}_{t+1}}(s_0)$ will yield higher rewards (see also figure 4). This is done following for the most part the various steps described in section 3.3, only one seeks in practice the optimal mapping $f_{\boldsymbol{\theta_{opt}}}$ such that $\boldsymbol{a}_{opt} \sim f_{\boldsymbol{\theta_{opt}}}(\boldsymbol{s_0})$, not the optimal set of actions $\boldsymbol{a}_{opt}$ itself, and the loss is computed from (26) by substituting a normalized averaged reward for the advantage function.

It is worth noticing that an accurate estimation of the policy gradient requires evaluating a large amount of actions drawn from the current policy, which comes at the expense of computing the same amount of reward evaluations. One key issue in the context of CFD applications is thus the ability to distribute a given set of actions to a parallel environment running on large computer clusters, as we show in the following that the CPU cost of solving the present steady-state optimization problems ranges from a few tens to several thousand hours.

The present workflow relies on the online PPO implementation of Stable Baselines, a toolset of reinforcement learning algorithms dedicated to the research community and industry [54], for which a custom OpenAI environment has been designed using the Gym library [55]. The instant reward r_t used to train the neural network is simply the quantity subjected to optimization (modulo a plus or minus sign to tackle both maximization and minimization problems). A moving average reward is also computed on the fly as the sliding average over the 100 latest values of r_t (or the whole sample if the latter has size smaller than 100). All other relevant hyper parameters are documented in the next sections, with the exception of the discount factor (since single-step PPO computes only one single reward per episode).

4 Control of natural convection in 2-D closed cavity

4.1 Case description

We address first the control of natural convection in the two-dimensional differentially heated square cavity schematically illustrated in figure 5(a). This is a widely studied benchmark system for thermally-driven flows,

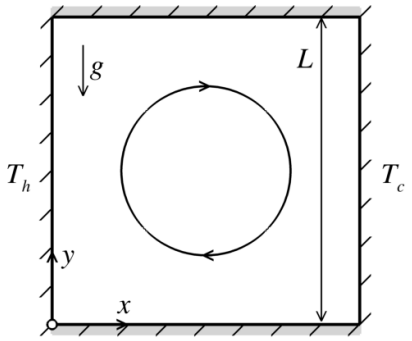

Figure 5: Schematic of the two-dimensional Rayleigh–Bénard set-up.

relevant in nature and technical applications (e.g., ocean and atmospheric convection, materials processing, metallurgy), that is thus suitable to validate and compare numerical solution algorithms while enriching the knowledge base for future projects in this field. A Cartesian coordinate system is used with origin at the lower-left edge, horizontal x-axis, and vertical y-axis. The cavity has side L, its top and bottom horizontal walls are perfectly insulated from the outside, and the vertical sidewalls are isothermal. Namely, the right sidewall is kept at a constant, homogeneous "cold" temperature T_c, and the left sidewall is entirely controllable via a constant in time, varying in space "hot" distribution $T_h(y)$ such that

$$\langle T_h \rangle > T_c \,, \tag{28}$$

where the brackets denote the average over space (here over the vertical position along the sidewall).

In the following, we neglect radiative heat transfer ($\chi = 0$) and consider a Boussinesq system driven by buoyancy, hence

$$\boldsymbol{\psi} = \rho_0 \beta (T - T_c) g \boldsymbol{e}_y \,, \tag{29}$$

where $\boldsymbol{g}$ is the gravitational acceleration parallel to the sidewalls, β is the thermal expansion coefficient, and we use the cold sidewall temperature as Boussinesq reference temperature. By doing so, the pressure featured in the momentum equation (2) and related weak forms must be understood as the pressure correction representing the deviation from hydrostatic equilibrium. The governing equations are solved with no-slip conditions $\boldsymbol{u} = \boldsymbol{0}$ on $\partial\Omega$ and temperature boundary conditions

$$\partial_y T(x,0,t) = \partial_y T(x,L,t) = 0 \,, \qquad T(0,y,t) = \langle T_h \rangle + \tilde{T}_h(y) \,, \qquad T(L,y,t) = T_c \,, \tag{30}$$

where $\tilde{T}_h$ is a zero-mean (in the sense of the average over space) distribution of hot temperature fluctuations subjected to optimization, whose magnitude is bounded by some constant ΔT_{max} according to

$$|\tilde{T}_h(y)| \leq \Delta T_{max} \,, \tag{31}$$

to avoid extreme and nonphysical temperature gradients. All results are made non-dimensional using the cavity side, the heat conductivity time, and the well-defined, constant in time difference between the averaged sidewall temperatures. The retained fluid properties yield values of the Rayleigh and Prandtl numbers

$$\mathrm{Ra} = \frac{g\beta(\langle T_h \rangle - T_c)L^3}{\nu\alpha} = 10^4 \,, \qquad \mathrm{Pr} = \frac{\nu}{\alpha} = 0.71 \,, \tag{32}$$

where $\alpha = \lambda/(\rho c_p)$ is the thermal diffusivity.

In order to assess the accuracy of the numerical framework, the uncontrolled solution has been computed by performing 60 iterations with time step $\Delta t = 0.5$ to march the initial solution (consisting of zero velocity and uniform temperature, except at the hot sidewall) to steady state. At each time step, an initially isotropic mesh is adapted under the constraint of a fixed number of elements $n_{el} = 4000$ using a multiple-component criterion featuring velocity and temperature, but no level-set. This is because the case is heat transfer but not conjugate heat transfer, as the solid is solely at the boundary $\partial\Omega$ of the computational domain, where either the temperature is known, or the heat flux is zero. It is thus implemented without the IVM and without a

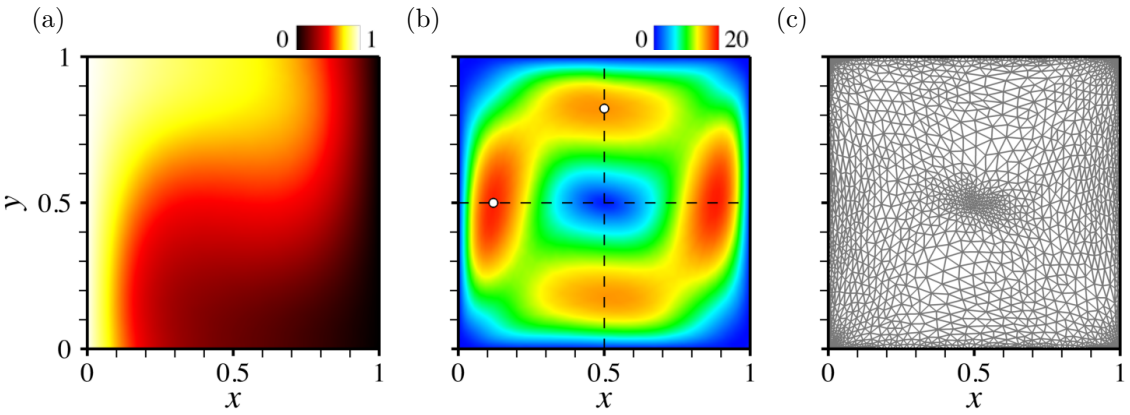

Figure 6: Iso-contours of the uncontrolled steady state (a) temperature and (b) velocity magnitude. (c) Adapted mesh. The circle symbols in (b) mark the positions of the maximum horizontal and vertical velocity along the centerlines reported in table 1.

		Present	Ref. [57]	Ref. [56]	Ref. [58]	Ref. [59]	Ref. [60]
$\mathrm{Ra} = 10^4$	Nu	2.267	2.245	2.238	2.201	2.245	2.245
	$\max u(0.5, y)$	16.048	16.179	16,178	–	16.262	16.178
	$y_{\max}$	0.823	0.824	0.823	0.832	0.818	0.827
	$\max v(x, 0.5)$	19.067	19.619	19.617	–	19.717	19.633
	$x_{\max}$	0.120	0.121	0.119	0.113	0.119	0.123

Table 1: Comparison of the present numerical results in the absence of control with reference benchmark solutions from the literature.

level set (although accurate IVM numerical solutions have been obtained in [40] using thick sidewalls with high thermal conductivity). The solution shown in figure 6(a,b) features a centered roll confined by the cavity walls, consistently with the fact that Ra exceeds the critical value $\mathrm{Ra}_c \sim 920$ for the onset of convection (as extrapolated from the near-critical benchmark data in [56]) by one order of magnitude, and heat transfer is thus driven by both conduction and convection. This shows in the Nusselt number, i.e., the non-dimensional temperature gradient averaged over the hot sidewall

$$\mathrm{Nu} = -\langle \partial_x T \rangle \,, \tag{33}$$

whose present value $\mathrm{Nu} = 2.27$ (as computed from 68 points uniformly distributed along the sidewall) exceeds that $\mathrm{Nu} = 1$ of the purely conductive solution, and exhibits excellent agreement with benchmark results from the literature. This is evidenced in table 1 where we also report the magnitude and position of the maximum horizontal velocity u (resp. the vertical velocity v) along the vertical centerline (resp. the horizontal centerline). The corresponding adapted mesh shown in figure 6(c) stresses that all boundary layers are sharply captured via extremely stretched elements, and that the adaptation strategy yields refined meshes near high temperature gradients and close to the side walls. Note however, the mesh refinement is not only along the boundary layers but also close to the recirculation regions near the cavity center, while the elements in-between are coarse and essentially isotropic.

4.2 Control

The question now being raised is whether DRL can be used to find a distribution of temperature fluctuations $\tilde{T}_h$ capable of alleviating convective heat transfer. To do so, we follow [27] and train a DRL agent in selecting piece-wise constant temperature distributions over n_s identical segments, each of which allows only two pre-determined states referred to as hot or cold. This is intended to reduce the complexity and the computational resources, as large/continuous action spaces are known to be challenging for the convergence of RL methods [61, 62]. Simply put, the network action output consists of n_s values $\hat{T}_{hk\in\{1\dots n_s\}} = \pm\Delta T_{max}$,

mapped into the actual fluctuations according to

$$\tilde{T}_{hk} = \frac{\hat{T}_{hk} - \langle \hat{T}_{hk} \rangle}{\max_l\{1, \dfrac{|\hat{T}_{hl} - \langle \hat{T}_{hl} \rangle|}{\Delta T_{max}}\}}\,, \tag{34}$$

to fulfill the zero-mean and upper bound constraints.[3] Ultimately, the agent receives the reward $r_t = -\mathrm{Nu}$ to minimize the space averaged heat flux at the hot sidewall.

All results reported herein are for $\Delta T_{max} = 0.75$ (so the hot temperature varies in the range $[0.25; 1.75]$) and $n_s = 10$ segments, as [27] report that $n_s = 20$ was computationally too demanding for their case, and that $n_s = 5$ yielded poor control efficiency. The agent is a fully-connected network with two hidden layers, each holding 2 neurons. The resolution process uses 8 environments and 2 steps mini-batches to update the network for 32 epochs, with learning rate 5×10^{-3}, and PPO loss clipping range $\epsilon = 0.2$.

4.3 Results

For this case, 120 episodes have been run, each of which follows the exact same procedure as above and performs 60 iterations with time step $\Delta t = 0.5$ to march the zero initial condition to steady state. This represents 960 simulations, each of which is performed on 4 cores and lasts 20s, hence 5h of total CPU cost. We present in figure 7 representative iso-contours of the steady-state temperature and velocity magnitude computed over the course of the optimization. The latter exhibit strong temperature gradients at the hot sidewall, together with a robust steady roll-shaped pattern accompanied by a small corner eddy at the upper-left edge of the cavity, whose size and position depends on the specifics of the temperature distribution. The corresponding meshes are displayed in figure 7(c) to stress the ability of the adaptation procedure to handle well the anisotropy of the solution caused by the intrinsic flow dynamics and the discontinuous boundary conditions.

We show in figure 8 the evolution of the controlled averaged Nusselt number, whose moving average decreases monotonically and reaches a plateau after about 90 episodes, although we notice that sub-optimal distributions keep being explored occasionally. The optimal computed by averaging over the 10 latest episodes (hence the 800 latest instant values) is $\langle \mathrm{Nu} \rangle_{\mathrm{opt}} \sim 0.57$, with variations ± 0.01 computed from the root-mean-square of the moving average over the same interval, which is a simple yet robust criterion to assess qualitatively convergence a posteriori. Interestingly, the optimized Nusselt number is almost twice as small as the purely conductive value ($\mathrm{Nu} = 1$), meaning that the approach successfully alleviates the heat transfer enhancement generated by the onset of convection, although it does not alleviates convection itself, as evidenced by the consistent roll-shaped pattern in figure 9. Similar results are reported in [27], for a different set-up in which the horizontal cavity walls are isothermal and control is applied at the bottom at the cavity (hence a different physics because of buoyancy), albeit with lower numerical and control efficiency since the authors report an optimal Nusselt number $\mathrm{Nu} \sim 1$ using up to 512 DRL environments with learning rate of 2.5×10^{-4}. The reason for such discrepancies probably lies in different ways of achieving and assessing control, as we use single-step PPO to optimize the steady-state Nusselt number via a time-independent control, which requires choosing a sidewall temperature, marching the controlled solution to steady state, then computing the reward. The problem considered in [27] is more intricate, as classic PPO is used to optimize the reward accumulated over time via a time-dependent control temperature updated with a certain period scaling with the convection time in the cavity (the so-determined optimal control being ultimately time-independent for the considered value of Ra, but truly time-dependent for Rayleigh numbers above $\sim 10^5$).

[3] Another possible approach would have been to penalize the reward passed to the DRL for those temperature distributions deemed non-admissible (either because the average temperature is non-zero or the temperature magnitude is beyond the threshold). However, this would have made returning admissible solutions part of the tasks the network is trained on (not to mention that non-zero average temperatures amount to a change in the Rayleigh number), which would likely have slowed down learning substantially.

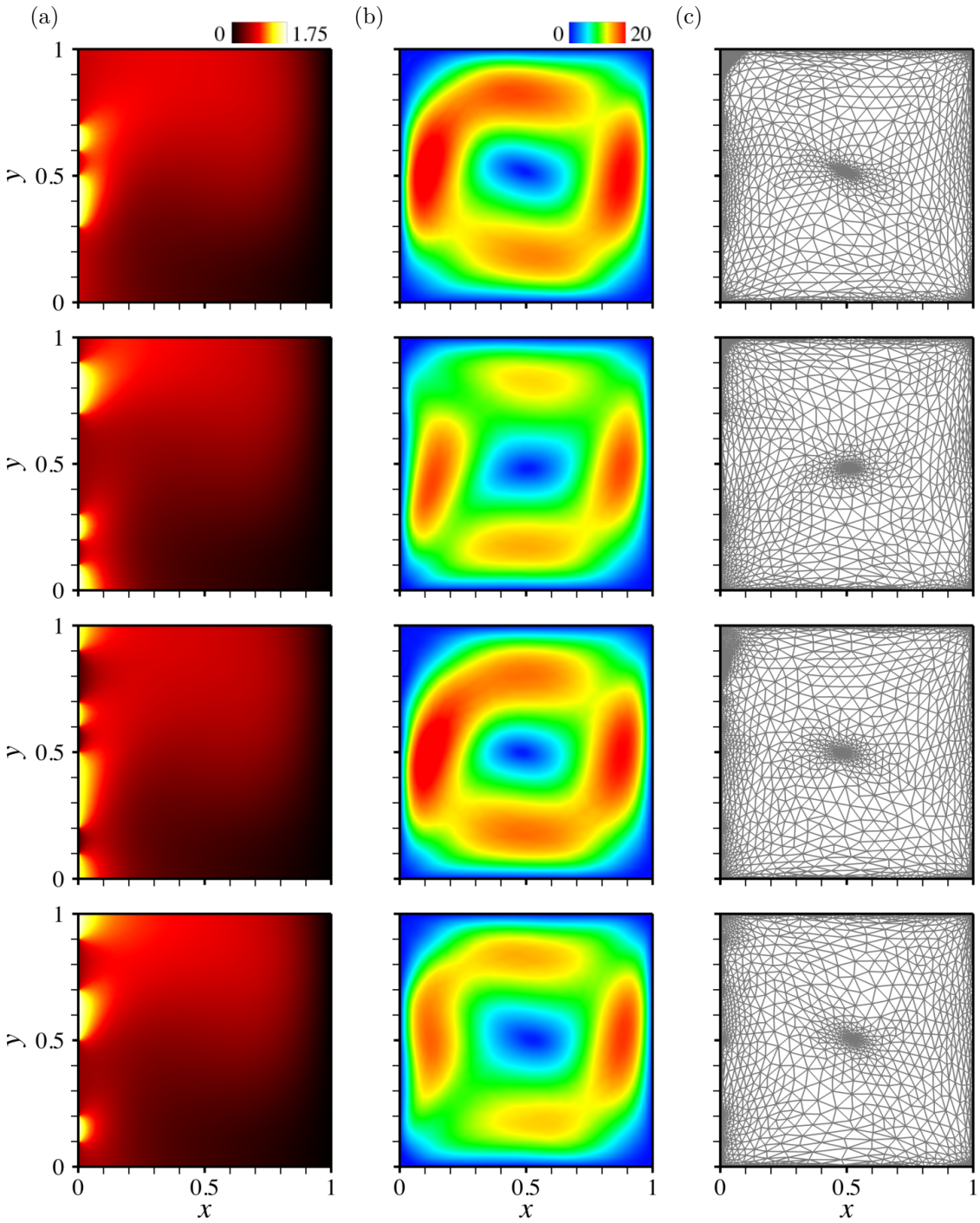

Figure 7: (a,b) Steady-state (a) temperature and (b) velocity magnitude against zero-mean temperature distributed at the left sidewall. (c) Adapted meshes.

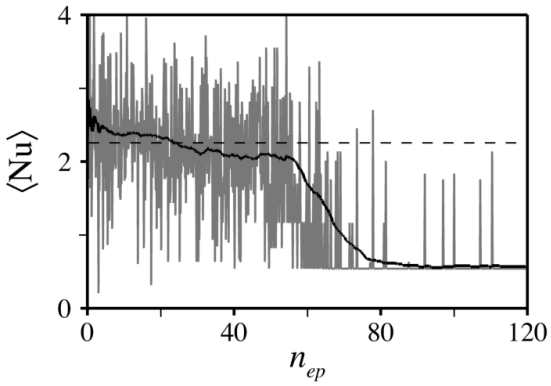

Figure 8: Evolution per learning episode of the instant (in grey) and moving average (in black) Nusselt number. The horizontal dashed line marks the uncontrolled value.

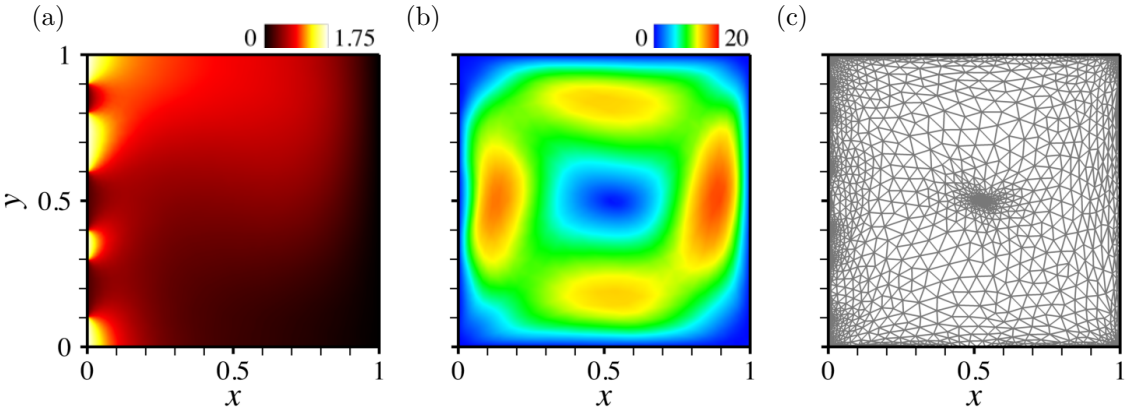

Figure 9: (a,b) Steady-state (a) temperature and (b) velocity magnitude for the optimal zero-mean temperature distribution. (c) Adapted mesh.

5 Control of forced convection in 2-D open cavity

5.1 Case description

This second test case addresses the control of actual conjugate heat transfer in a model setup for the cooling of a hot solid by impingement of a fluid; see figure 10(a). A Cartesian coordinate system is used with origin at the center of mass of the solid, horizontal x-axis, and vertical y-axis. The solid has rectangular shape with height h and aspect ratio 2:1, and is initially at the hot temperature T_h. It is fixed at the center of a rectangular cavity with height H and aspect ratio 4:1, whose walls are isothermal and kept at temperature T_w. The top cavity side is flush with n_j identical holes of width e_i whose distribution is subjected to optimization, each of which models the exit plane of an injector blowing cold air at velocity V_i and temperature T_c, and is identified by the horizontal position of its center $x_{k\in\{1\dots n_j\}}$. In order to allow releasing hot air from the cavity, the sidewalls are blown with two identical exhaust areas of height e_o, identified by the vertical position of their center $(e_0 - H)/2$.

For this case, both buoyancy and radiative heat transfer are neglected (hence, $\boldsymbol{\psi} = \mathbf{0}$ and $\chi = 0$), meaning that temperature evolves as a passive scalar, similar to the mass fraction of a reactant in a chemical reaction. All relevant parameters are provided in Table 2, including the material properties used to model the composite fluid, that yield fluid values of the Reynolds and Prandtl numbers

$$\mathrm{Re} = \frac{\rho V_i e}{\mu} = 200\,, \qquad \mathrm{Pr} = 2\,. \tag{35}$$

(a) (b)

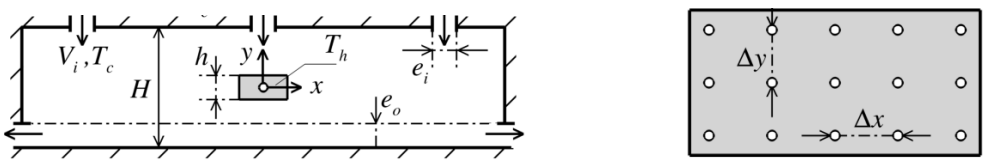

Figure 10: (a) Schematic of the 2-D forced convection set-up. (b) Sensors positions in the solid domain.

H	h	e_i	e_o	V_i	T_w	T_c	T_h
1	0.2	0.2	0.2	1	10	10	150

	μ	ρ	λ	c_p
fluid	0.001	1	0.5	1000
solid	1000	100	15	300

Table 2: Numerical parameters used in the 2-D forced convection problem. All values in SI units, with the exception of temperatures given in Celsius.

Note the very high value of the ratio of the solid to fluid viscosities, that ensures that the velocity is zero in the solid domain and that the no-slip interface condition is satisfied. By doing so, the convective terms drop out in the energy equation, that reduces to the pure conduction equation for the solid. The governing equations are solved with no-slip isothermal conditions $\boldsymbol{u} = \boldsymbol{0}$ and $T = T_w$ on $\partial\Omega$, except at the injection exit planes ($\boldsymbol{u} = -V_i \boldsymbol{e}_y$, $T = T_c$), and at the exhaust areas, where a zero-pressure outflow condition is imposed ($p = \partial_x u = \partial_x T = 0$). No thermal condition is imposed at the interface, where heat exchange is implicitly driven by the difference in the individual material properties.

5.2 Control

The quantity being optimized is the distribution of the injectors center positions $x_{k\in\{1\dots n_j\}}$, each of which is forced to sit in an interval $[x_k^-; x_k^+]$ whose edge values are determined beforehand of recomputed on the fly (depending on the control strategy), and bounded according to

$$|x_k^\pm| \leq x_m \,, \tag{36}$$

where we set $x_m = 2H - 0.75e_i$ to avoid numerical issues at the upper cavity edges. The network action output therefore consists of n_j values $\hat{x} \in [-1; 1]$, mapped into the actual positions according to

$$x_k = \frac{x_k^+(\hat{x}_k + 1) - x_k^-(\hat{x}_k - 1)}{2} \,. \tag{37}$$

In order to compute the reward passed to the DRL, we distribute uniformly 15 probes in the solid domain, into $n_x = 5$ columns and $n_y = 3$ rows with resolutions $\Delta x = 0.09$ and $\Delta y = 0.075$, respectively; see figure 10(b). Selected tests have been carried out to check that the outcome of the learning process does not change using $n_y = 5$ rows of $n_x = 5$ probes (not shown here). The magnitude of the tangential heat flux is estimated by averaging the norm of the temperature gradient over all columns and rows, i.e., i-th column (resp. the j-th row) as

$$\langle||\nabla_\parallel T||\rangle_i = \frac{2}{n_y - 1} |\sum_{j\neq 0} \mathrm{sgn}(j) ||\nabla T||_{ij}| \,, \qquad \langle||\nabla_\parallel T||\rangle_j = \frac{2}{n_x - 1} |\sum_{i\neq 0} \mathrm{sgn}(i) ||\nabla T||_{ij}| \,, \tag{38}$$

where subscripts i, j and ij denote quantities evaluated at $x = i\Delta x$, $y = j\Delta y$ and $(x, y) = (i\Delta x, j\Delta y)$, respectively, and symmetrical numbering is used for the center probe to sit at the intersection of the zero-th column and row. The numerical reward $r_t = -\langle||\nabla_\parallel T||\rangle$ fed to the DRL agent deduces ultimately by averaging over all rows and columns, to give

$$\langle||\nabla_\parallel T||\rangle = \frac{1}{n_x + n_y} \sum_{i,j} \langle||\nabla_\parallel T||\rangle_i + \langle||\nabla_\parallel T||\rangle_j \,, \tag{39}$$

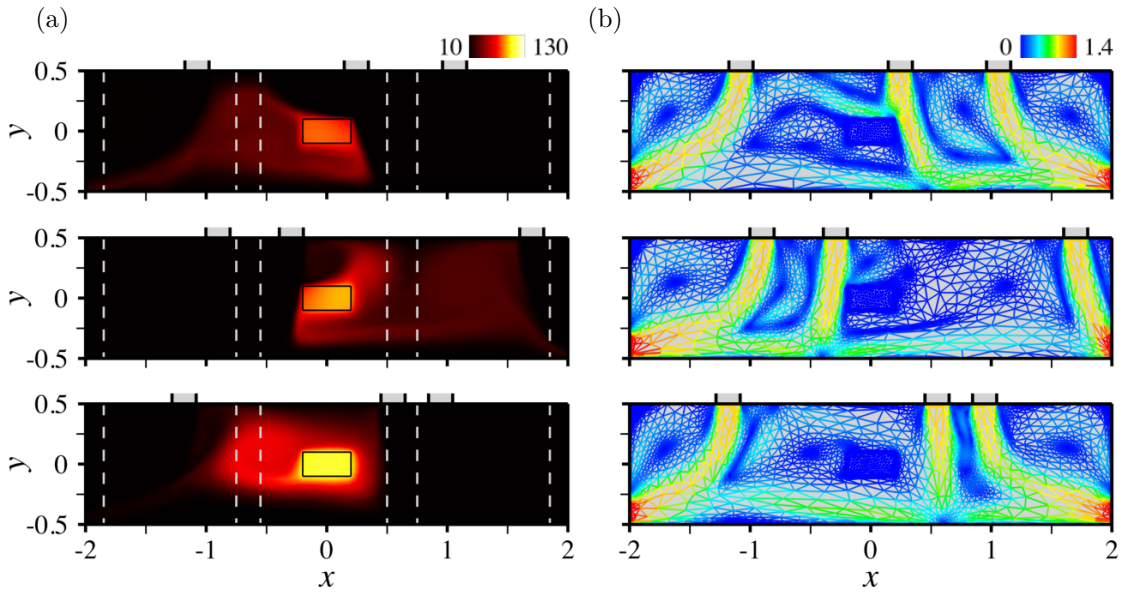

Figure 11: (a) Steady-state temperature against arrangements of 3 injectors, with admissible values under the fixed domain decomposition strategy S_1 delimited by the dashed lines. (b) Adapted meshes colored by the magnitude of velocity.

which especially yields $r_t = 0$ for a perfectly homogeneous cooling.

All results reported in the following are for $n_j = 3$ injectors. The agent is a fully-connected network with two hidden layers, each holding 2 neurons. The resolution process uses 8 environments and 2 steps mini-batches to update the network for 32 epochs, with learning rate set to 5×10^{-3}, and PPO loss clipping range to $\epsilon = 0.3$.

5.3 Results

5.3.1 Fixed domain decomposition strategy

We consider first the so-called fixed domain decomposition strategy S_1 in which the top cavity wall is split into n_j equal subdomains, and each injector is forced to sit in a different subdomain. The edge values for the position x_k of the k-th injector read

$$x_k^- = -x_m + (k-1)\frac{2x_m + e_i}{n_j}\,, \qquad x_k^+ = x_k^- + \frac{2x_m - (n_j - 1)e_i}{n_j}\,. \tag{40}$$

It can be checked that $x_k^- = x_{k-1}^+ + e_i$, so it is possible to end up with two side-by-side injectors, which is numerically equivalent to having $n_j - 1$ injectors, $n_j - 2$ of width e_i plus one of width $2e_i$. For this case, 60 episodes have been run, each of which performs 1500 iterations with time step $\Delta t = 0.1$ to march the same initial condition (consisting of zero velocity and uniform temperature, except in the solid domain) to steady state, using the level set, velocity and temperature as multiple-component criterion to adapt the mesh (initially pre-adapted using the sole level set) every 5 time steps under the constraint of a fixed number of elements $n_{el} = 15000$. This represents 480 simulations, each of which is performed on 8 cores and lasts 10mn, hence 80h of total CPU cost.

It is out of the scope of this work to analyze in details the many flow patterns that develop when the blown fluid travels through the cavity. Suffice it to say that the outcome depends dramatically on the injectors arrangement, and features complex rebound phenomena (either fluid/solid, when a jet impinges on the cavity walls or on the workpiece itself, or fluid/fluid, when a deflected jet meets the crossflow of another jet), leading to the formation of multiple recirculations varying in number, position and size. Several such cases are illustrated in figure 11 via iso-contours of the steady-state temperature distributions, together with the

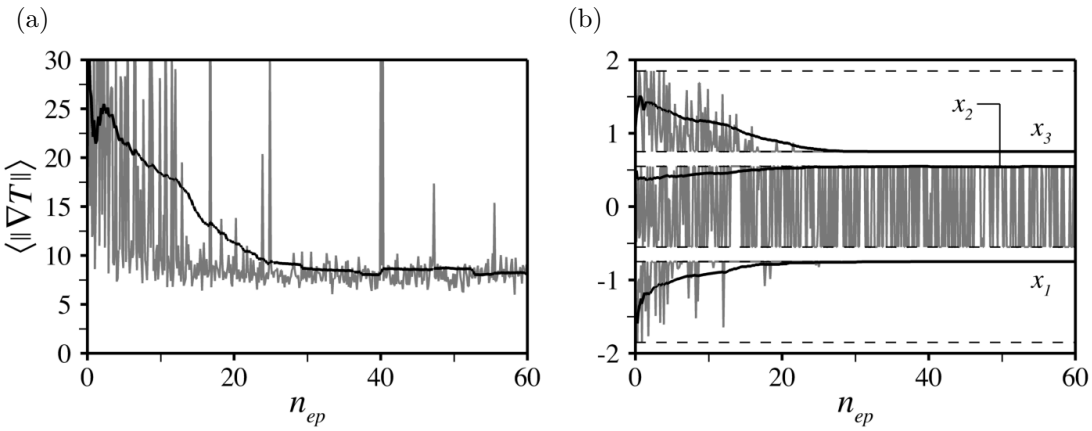

Figure 12: (a) Evolution per learning episode of the instant (in grey) and moving average (in black) rewards under the fixed domain decomposition strategy S_1. (b) Same as (a) for the injectors center positions, with admissible values delimited by the dashed lines.

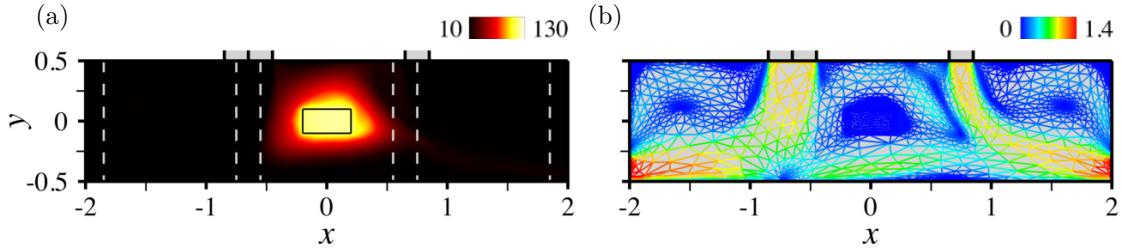

Figure 13: Same as figure 11 for the optimal arrangement of 3 injectors under the fixed domain decomposition strategy S_1.

corresponding adapted meshes colored by the magnitude of velocity to illustrate the ability of the numerical framework to capture accurately all boundary layers and shear regions via extremely stretched elements.

One point worth being mentioned is that the individual position signals are best suited to draw robust quantitative conclusion, as there is noise in the reward signal shown in figure 12(a). The issue, we believe, is twofold: on the one hand, the reward is approximated from pointwise temperature data (similar to experimental measurements) that are more sensitive to small numerical errors (e.g., the interpolation error at the probes position) than an integral quantity. On the other hand, the mesh adaptation procedure is not a deterministic process, as the outcome depends on the processors and number of processors used, and any initial difference propagates over the course of the simulation because the meshes keep being adapted dynamically. In return, two exact same control parameters can thus yield different rewards on behalf of different interpolation errors at the probes position. This likely slows down learning and convergence, but we show in figure 12(b) that the moving average distribution does converge to an optimal arrangement after roughly 25 episodes. The latter consists of an injector at the right-end of the left subdomain ($x_{1\text{opt}} = -0.75$) and two side-by-side injectors sitting astride the center and right subdomains ($x_{2\text{opt}} = 0.55$ and $x_{3\text{opt}} = 0.75$), that enclose the workpiece in a double-cell recirculation; see figure 13. These values have been computed by averaging the instant positions of each injector over the 10 latest episodes, with variations ± 0.002 computed from the root-mean-square of the moving average over the same interval, a procedure that will be used consistently to assess convergence for all cases reported in the following. The efficiency of the control itself is estimated by computing the magnitude of tangential heat flux averaged over the same interval, found to be $\langle ||\nabla_{\parallel} T|| \rangle_{\text{opt}} \sim 8.3$. Note, the position $x_{2\text{opt}}$ is actually obtained by averaging the absolute value of the instant position x_2 (although the true, signed value is depicted in the figure), which is because the center injector keeps oscillating between two end positions ± 0.55 on behalf of reflectional symmetry with respect to the vertical centerline.

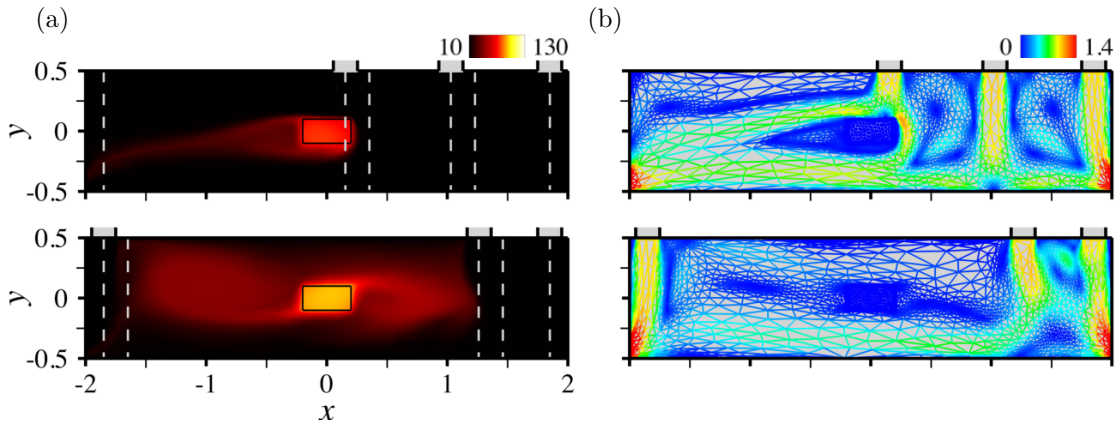

Figure 14: (a) Steady-state temperature against arrangements of 3 injectors, with admissible values under the follow-up strategy S_2 delimited by the dashed lines. (b) Adapted meshes colored by the magnitude of velocity.

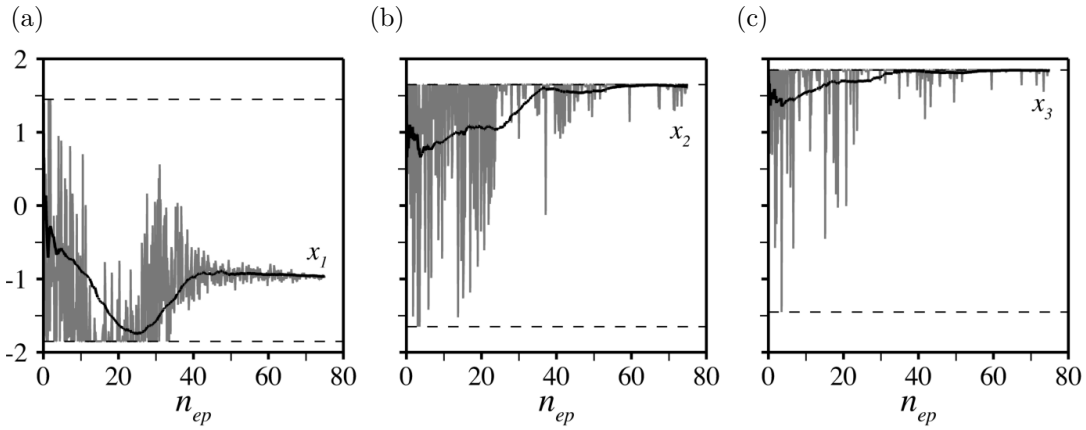

Figure 15: Evolution per learning episode of the instant (in grey) and moving average (in black) injectors center positions under the follow-up strategy S_2, with admissible values delimited by the dashed lines.

5.3.2 Follow-up strategy

We consider now the so-called follow-up strategy S_2, in which all injectors are distributed sequentially the ones with respect to the others. The corresponding edge values

$$x_1^- = -x_m\,, \qquad x_1^+ = x_m - (n_j - 1)e_i\,, \tag{41}$$

$$x_k^- = x_{k-1}^+ + e_i\,, \qquad x_k^+ = x_m - (n_j - k)e_i\,, \tag{42}$$

readily express that the k-th injector is forced to sit between the $k-1$-th one and the upper-right cavity edge while leaving enough space to distribute the remaining $n_j - k$ injectors, which increases the size of the control parameter space while again leaving the possibility for side-by-side injectors (since $x_k^- = x_{k-1}^+ + e_i$ by construction). 75 episodes have been run for this case following the exact same procedure as above, i.e., marching the zero initial condition in time up to $t = 150$ with $\Delta t = 0.1$, hence 600 simulations, each of which is performed on 8 cores and lasts 10mn, hence 100h of total CPU cost.

When it comes to the computed flow patterns, the results closely resemble those obtained under the previous fixed domain decomposition strategy, although figure 14 exhibits increased dissymmetry when two or more injectors move simultaneously to the same side of the cavity. We show in figure 15 that the moving average distribution converges after roughly 60 episodes, with the optimal arrangement consisting of one injector roughly midway between the left cavity sidewall and the workpiece ($x_{1\text{opt}} = -0.96$), and two side-by-side injectors at the right end of the cavity ($x_{2\text{opt}} = 1.65$ and $x_{3\text{opt}} = 1.85$). The variations over the same interval

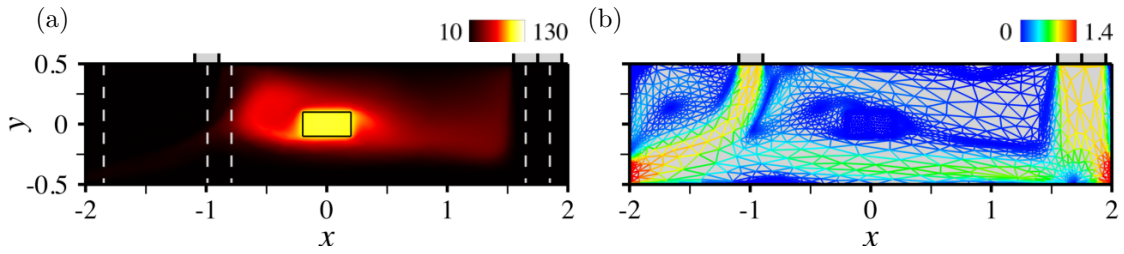

Figure 16: Same as figure 14 for the optimal arrangement of 3 injectors under the follow-up strategy S_2.

are by ± 0.006; see also figure 16 for the corresponding flow pattern. Convergence here is much slower than under S_1, as the search for an optimal is complicated by the fact that all injector positions are interdependent the ones on the others and it is up to the network to figure out exactly how. Another contingent matter is that the agent initially spans a fraction of the control parameter space because the large values of x_1 considered limit the space available to distribute the other two injectors. This is all the more so as such configurations turn to be far from optimality, for instance the magnitude of tangential heat flux is $\langle ||\nabla_\parallel T|| \rangle \sim 41.3$ for $x_1 = 1.45$, $x_2 = 1.65$ and $x_3 = 1.85$, but $\langle ||\nabla_\parallel T|| \rangle_{\rm opt} \sim 6.3$ at optimality. The latter value is smaller than the optimal achieved under S_1, consistently with the fact that all positions spanned under S_1 are admissible under S_2, hence the S_1 optimal is expected to be a S_2 sub-optimal.

5.3.3 Free strategy

We examine now a third strategy S_3 referred to as the free strategy, in which all injectors are independent and free to move along the top cavity wall. The edge values for the position x_k of the k-th injector read

$$x_k^- = -x_m \,, \qquad\qquad x_k^+ = x_m \,, \tag{43}$$

so two injectors can end up side-by side and even overlapping one another if $|x_l - x_m| < e_i$. If so, we implement a single injector of width $e_i + |x_l - x_m|$ and maintain the blowing velocity (not the flow rate) for the purpose of automating the set-up design process, meaning that having n_j injectors, two of which overlap exactly (i.e., $|x_l - x_m| = 0$) is rigorously equivalent to having $n_j - 1$ injectors. 60 episodes have been run for this case following the exact same procedure as above.

All flow patterns are reminiscent of those obtained under the previous fix decomposition S_1 and follow-up S_2 strategies, even when two injectors overlap; see figure 17. Other than that, we show in figures 18 that the moving average distribution converges to an optimal consisting of two injectors almost perfectly overlapping one another at the left end of the cavity ($x_{1\rm opt} = -1.85$ and $x_{2\rm opt} = -1.82$), and a third injector at the right end of the cavity ($x_{3\rm opt} = 1.85$). The variations over the same interval are by ± 0.007, and the associated flow pattern shown in figure 19 is symmetrical and features two large recirculations on either side of the workpiece. Convergence occurs after roughly 40 episodes, i.e., faster than under S_2 (consistently with the fact that there is no need to learn anymore about how the network outputs depend the ones on the others) but slower than under S_1 (consistently with the fact that the size of the control parameter space has increased substantially). It is worth noticing that the system is invariant by permutations of the network outputs, meaning that there exist $2^{n_j} - 2$ distributions (hence 6 for $n_j = 3$) associated with the same reward. Nonetheless, a single optimal is selected, which is essentially fortuitous since the agent does not learn about symmetries under the optimization process (otherwise S_1 would have similarly selected a single optimal). The magnitude of tangential heat flux is $\langle ||\nabla_\parallel T|| \rangle_{\rm opt} \sim 11.2$ at optimality, i.e., larger than that achieved under S_2. This can seem surprising at first, because all positions spanned under S_2 are admissible under S_3, and the S_2 optimal is thus expected to be a S_3 sub-optimal. However, the argument does not hold here because the overlap in the S_3 optimal reduces the flow rate to that of a two-injectors set-up, so the comparison should be with the S_2 optimal with $n_j = 2$.

5.3.4 Inverse strategy

Finally, we propose here to make the most of the numerical framework flexibility to solve a different optimization problem consisting in selecting first an injector distribution, then in finding which position x_0 of the solid center of mass minimizes the magnitude of the tangential heat flux defined by (38)-(39). The

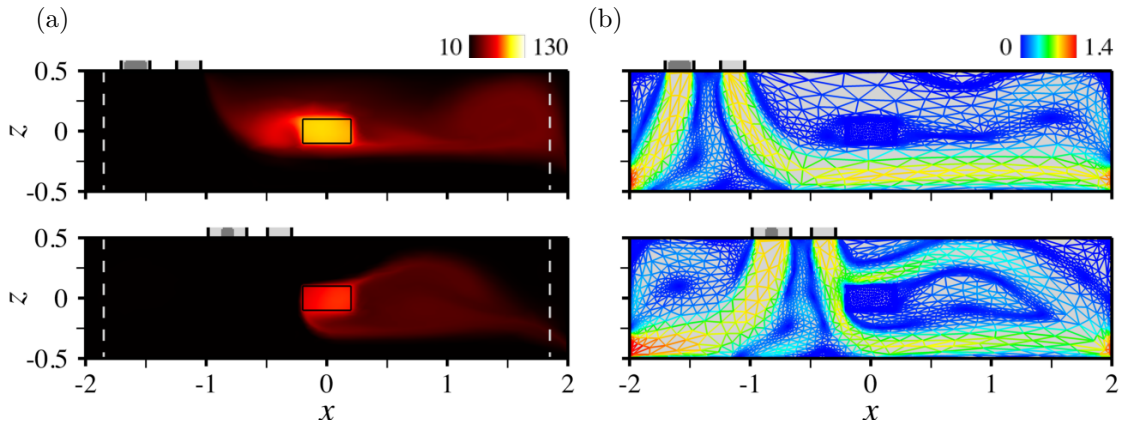

Figure 17: (a) Steady-state temperature against arrangements of 3 injectors, with admissible values under the free strategy S_3 delimited by the dashed lines and overlaps marked by the dark grey shade. (b) Adapted meshes colored by the magnitude of velocity.

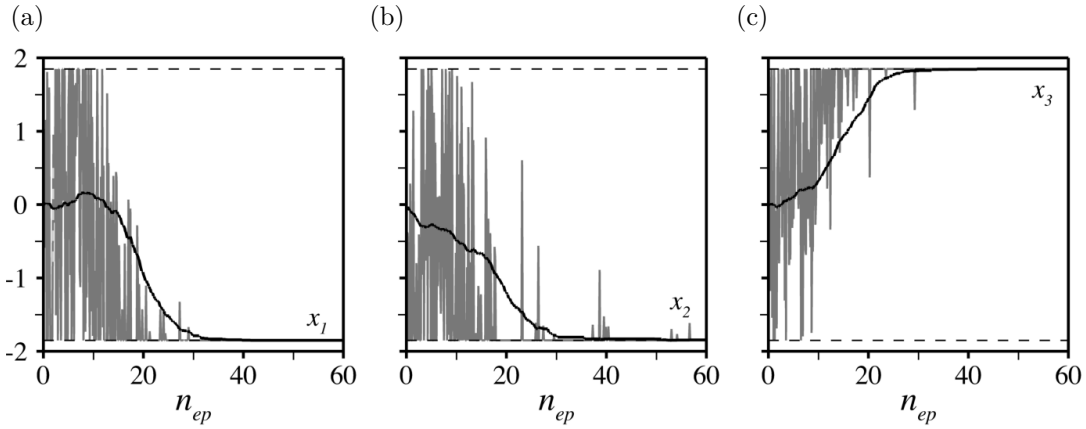

Figure 18: Evolution per learning episode of the instant (in grey) and moving average (in black) injectors center positions under the free strategy S_3, with admissible values delimited by the dashed lines.

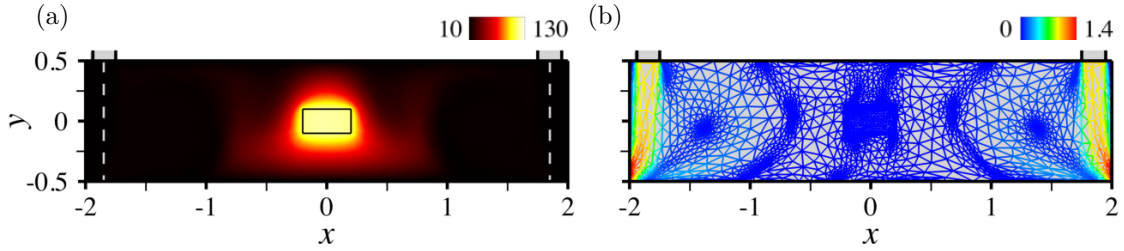

Figure 19: Same as figure 17 for the optimal arrangement of 3 injectors under the free strategy S_3.

so-called inverse strategy S_4 considered herein features two injectors at each end of the cavity ($x_1 = -1.85$ and $x_2 = 1.85$), identical to the optimal arrangement of 3 injectors under the free strategy S_3. The center of mass can take any value in $[-x_{0m}; x_{0m}]$ where we set $x_{0m} = 2(H - h)$ to avoid numerical issues at the sidewalls. The same coordinate system as above is used, but with reference frame attached to the cavity, not the moving solid (hence all results obtained under the previous strategies pertain to $x_0 = 0$ in the new system).

A total of 60 episodes have been run for this case using the exact same DRL agent, the only difference being in the network action output, now made up of a single value $\hat{x}_0 \in [-1; 1]$, mapped into the actual position

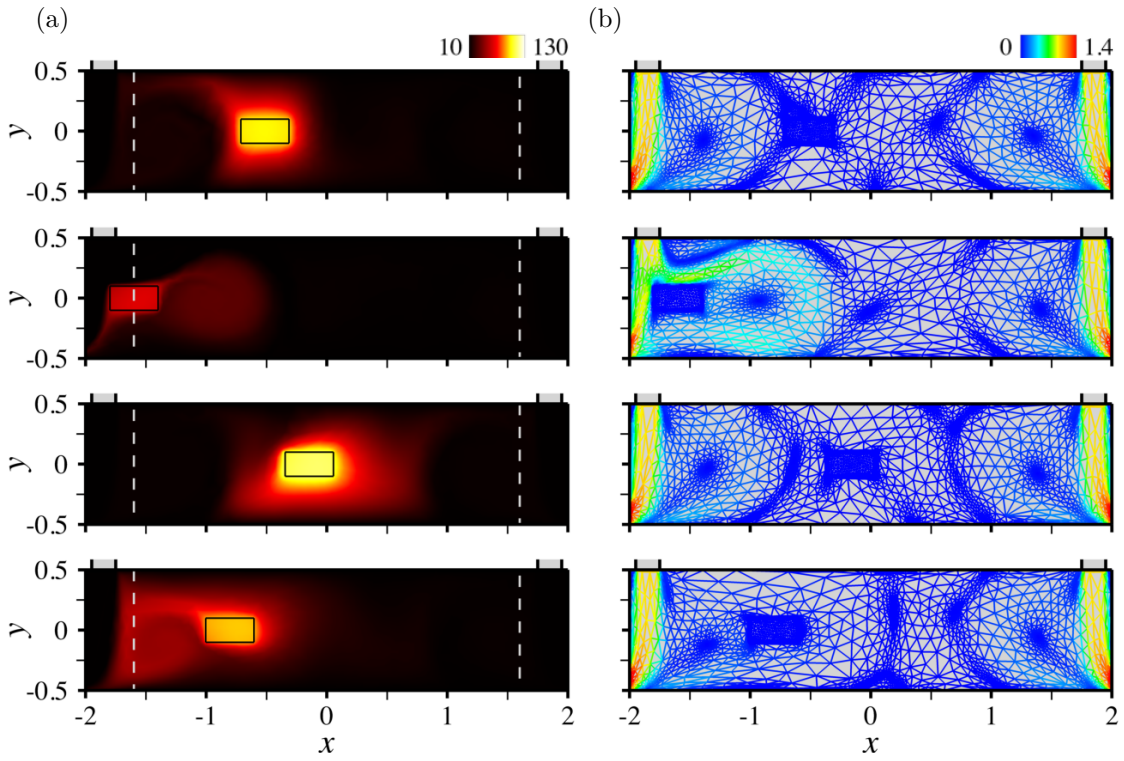

Figure 20: (a) Steady-state temperature against solid center of mass position, with admissible domains under the inverse strategy S_4 marked by the dashed lines. (b) Adapted meshes colored by the norm of velocity.

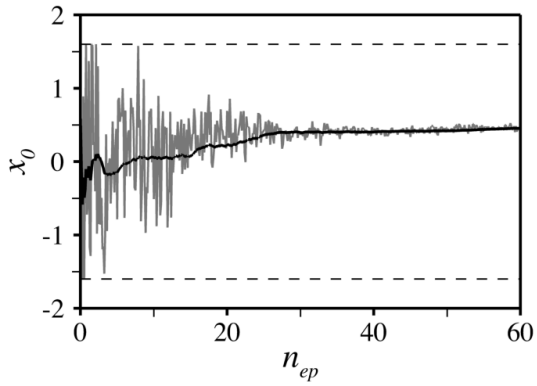

Figure 21: Evolution per learning episode of the instant (in grey) and moving average (in black) center of mass positions under the inverse strategy S_4, with admissible values delimited by the dashed lines.

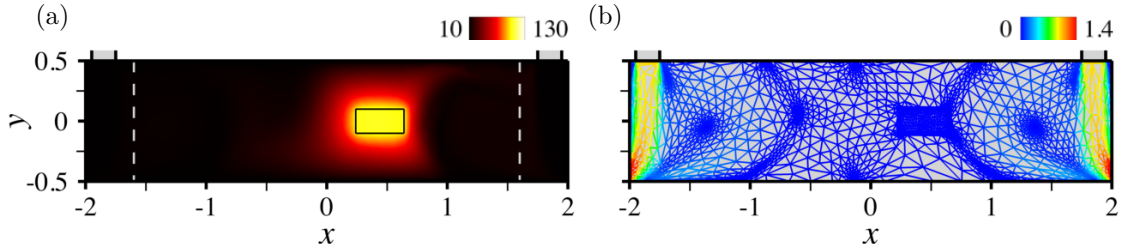

Figure 22: Same as figure 20 for the optimal center of mass position under the inverse strategy S_4.

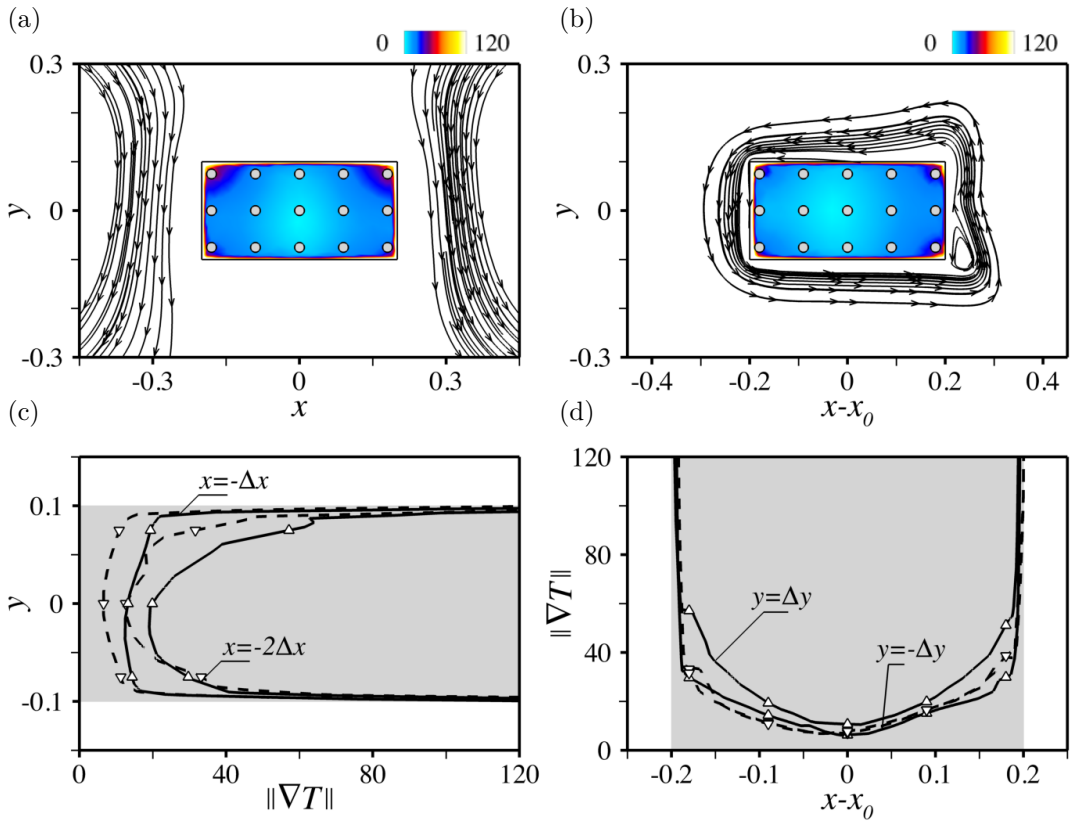

Figure 23: (a,b) Norm of the temperature gradient in the solid domain with superimposed streamlines of the underlying velocity field, as computed for (a) $x_0 = 0$, and (b) $x_{0\text{opt}} = 0.45$, i.e., the optimal position selected under the inverse strategy S_4. (c) Cuts along the two leftmost columns of probes. The solid and dashed lines refer to $x_0 = 0$ and $x_{0\text{opt}} = 0.45$, respectively, and the symbols mark the probe values. (d) Same as (c) for cuts along the lower and upper rows of columns.

using

$$x_0 = x_{0m}\hat{x}_0\,. \tag{44}$$

A large variety of flow patterns is obtained by doing so, that closely resemble those computed under the previous strategies, only the outcome is now also altered by the width of the gap between the cavity sidewalls and the workpiece, as illustrated in figure 20. We show in figure 21 that the position of the solid center of mass converges to an optimal position $x_{0\text{opt}} = 0.42$ (the variations over the same interval being by ± 0.005), the associated magnitude of tangential heat flux $\langle ||\nabla_{\parallel} T|| \rangle_{\text{opt}} \sim 4.1$, being smaller than that achieved under S_3 using a centered workpiece. The fact that the optimal position is offset from the horizontal centerline is a little surprising at first, because intuition suggests that the simplest way to achieve homogeneous heat transfer is by having injectors symmetrically distributed with respect to the vertical centerline. Nonetheless, examining carefully the norm of the temperature gradient in the solid domain shows that $x_0 = 0$ achieves close to perfect horizontal symmetry but vertical asymmetry, owing to the formation of two large-scale, small velocity end vortices entraining heat laterally downwards; see figure 23(a). Conversely, for $x \sim x_{0\text{opt}}$, the workpiece it almost at the core of the closest recirculation region, hence the surrounding fluid particles have small velocities and wrap almost perfectly around its surface, as illustrated in figure 23(b). This restores excellent vertical symmetry, as evidenced by relevant cuts along the two leftmost columns of probes in figure 23(c), and along the lower and upper rows in figure 23(d), which explains the improved the reward.

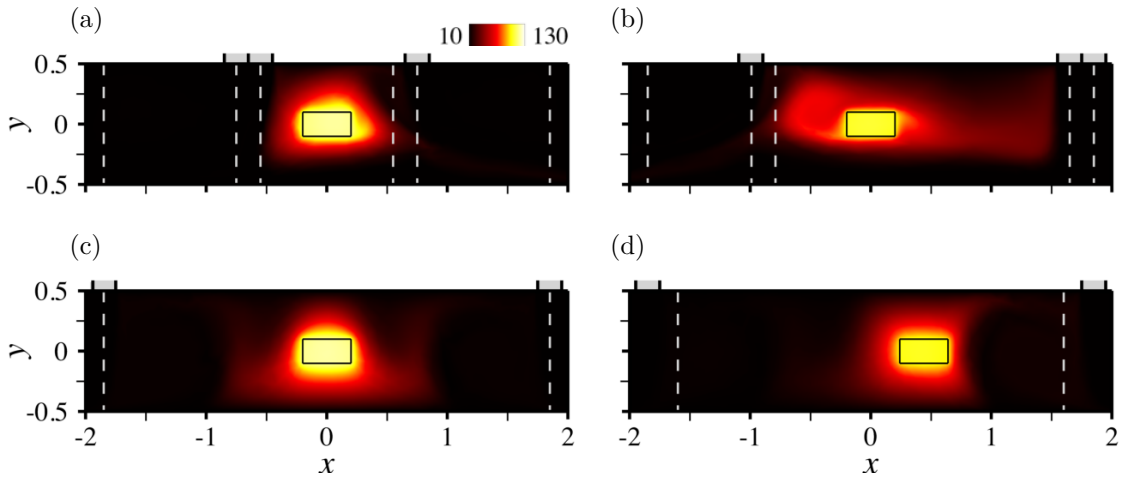

Figure 24: (a-c) Optimal arrangements of 3 injectors under the (a) fixed decomposition domain strategy S_1, (b) follow-up strategy S_2 and (c) free strategy S_3. (b) Optimal position of the workpiece under the inverse strategy S_4.

	n_j	n_{ep}	x_0	x_1	x_2	x_3	$\langle\|\|\nabla_\parallel T\|\|\rangle$
S_1	3	60	0	-0.75	± 0.55	0.75	8.3
S_2	3	75	0	-0.96	1.65	1.85	6.3
S_3	3	60	0	-1.85	-1.82	1.85	11.2
S_4	2	60	0.42	-1.85	1.85	–	4.1

Table 3: Numerical data for the optimal arrangements computed under strategies S_{1-4}. All values computed by averaging the instant signal over the 10 latest learning episodes.

5.4 Discussion

Figure 24 reproduces the optimal temperature distributions computed under the various strategies considered above. For benchmarking purposes, we also provide in table 3 relevant convergence data computed over the 10 latest episodes. To recap, the most homogeneous cooling is achieved under the follow-up strategy S_2, but the DRL agent seems more easily trained under the fixed decomposition domain strategy S_1 and the free strategy S_3. Another interesting point is the extent to which the workpiece is actually cooled, for which S_2 seems more relevant, on behalf of the dissymmetry in the left and right flow rates that creates order one velocities at the bottom of the cavity. This stresses S_2 as a possible compromise to achieve efficient *and* homogeneous cooling, although a true optimal with this regards can be computed rigorously by applying the same approach to compound functionals weighing, e.g., the magnitude of the tangential heat flux and the solid center temperature (which we defer to future work).

These results provide a basis for future self-assessment of the method and identifies potential for improvement regarding the convergence efficiency. The approach can certainly benefit from a fine tuning of the reward computation, as having sufficient spatial resolution on the relevant state of the system is an obvious requirement to allow a successful control. Adjusting the trade-off between exploration and exploitation is also worth consideration to better handle the existence of multiple global optima (whether they stem from symmetries of from the topology of the reward itself) which could be done using non-normal probability density functions.

6 Extension to 3-D forced convection

6.1 Case description

The model cooling set up considered in section 5 is extended here to 3-D to assess the extent to which the approach carries over to three-dimensional conjugate heat transfer. The main differences between 2-D and 3-D are as follows: a Cartesian coordinate system is used with origin at the center of mass of the solid,

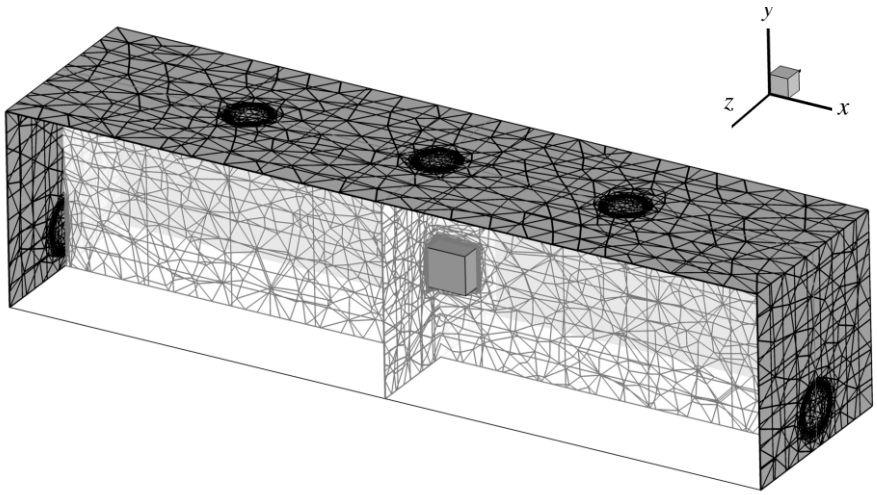

Figure 25: Schematic of the 3-D forced convection set-up.

H	h	d_i	d_o	δ_o	V_i	T_w	T_c	T_h
1	0.2	0.2	0.24	0.16	1	10	10	150

	μ	ρ	λ	c_p
fluid	0.01	1	0.5	1000
solid	1000	100	15	300

Table 4: Numerical parameters used in the 3-D forced convection problem. All values in SI units, with the exception of temperatures given in Celsius.

horizontal x-axis, vertical y-axis, and the z-axis completes the direct triad; see figure 25. The solid is a rectangular prism with aspect ratio 2:1:1, and is fixed at the center of a rectangular cavity with height H and aspect ratio 4:1:1. We consider n_j circular-shaped injectors with diameter d_i, whose exit planes are forced to be symmetrical with respect to $z = 0$, hence each injector is identified by the horizontal position of its center $x_{k\in\{1\dots n_j\}}$. We also use circular-shaped exhaust areas with diameter d_o, offset by a distance δ_o from the bottom of the cavity, and whose exit planes are also symmetrical with respect to $z = 0$, hence each exhaust area is identified by the vertical position of its center $(d_0 + \delta_o - H)/2$. The governing equations are solved with the exact same boundary conditions as in section 5. All parameters are provided in Table 4, including the material properties used to model the composite fluid, that yield fluid values of the Reynolds and Prandtl numbers

$$\mathrm{Re} = \frac{\rho V_i d_i}{\mu} = 20\,, \qquad\qquad \mathrm{Pr} = 20\,. \tag{45}$$

6.2 Control strategy

We keep here the same control objective and compute the reward fed to the DRL from 45 probes arranged symmetrically into $n_z = 3$ transverse layers with resolution $\Delta z = 0.075$, each of which distributes uniformly 15 probes into $n_x = 5$ columns and $n_y = 3$ rows with resolutions $\Delta x = 0.09$ and $\Delta y = 0.075$. In practice, the 3-D reward is simply the average over z of the 2-D reward defined in section 5, hence $r_t = -\langle||\nabla_\parallel T||\rangle$ with

$$\langle||\nabla_\parallel T||\rangle = \frac{1}{(n_x+n_y)n_z}\sum_{i,j,k}\langle||\nabla_\parallel T||\rangle_{ik} + \langle||\nabla_\parallel T||\rangle_{jk}\,, \tag{46}$$

with

$$\langle||\nabla_\parallel T||\rangle_{ik} = \frac{2}{n_y-1}\Big|\sum_{j\neq 0}\mathrm{sgn}(j)||\nabla T||_{ijk}\Big|\,, \qquad \langle||\nabla_\parallel T||\rangle_{jk} = \frac{2}{n_x-1}\Big|\sum_{i\neq 0}\mathrm{sgn}(i)||\nabla T||_{ijk}\Big|\,, \tag{47}$$

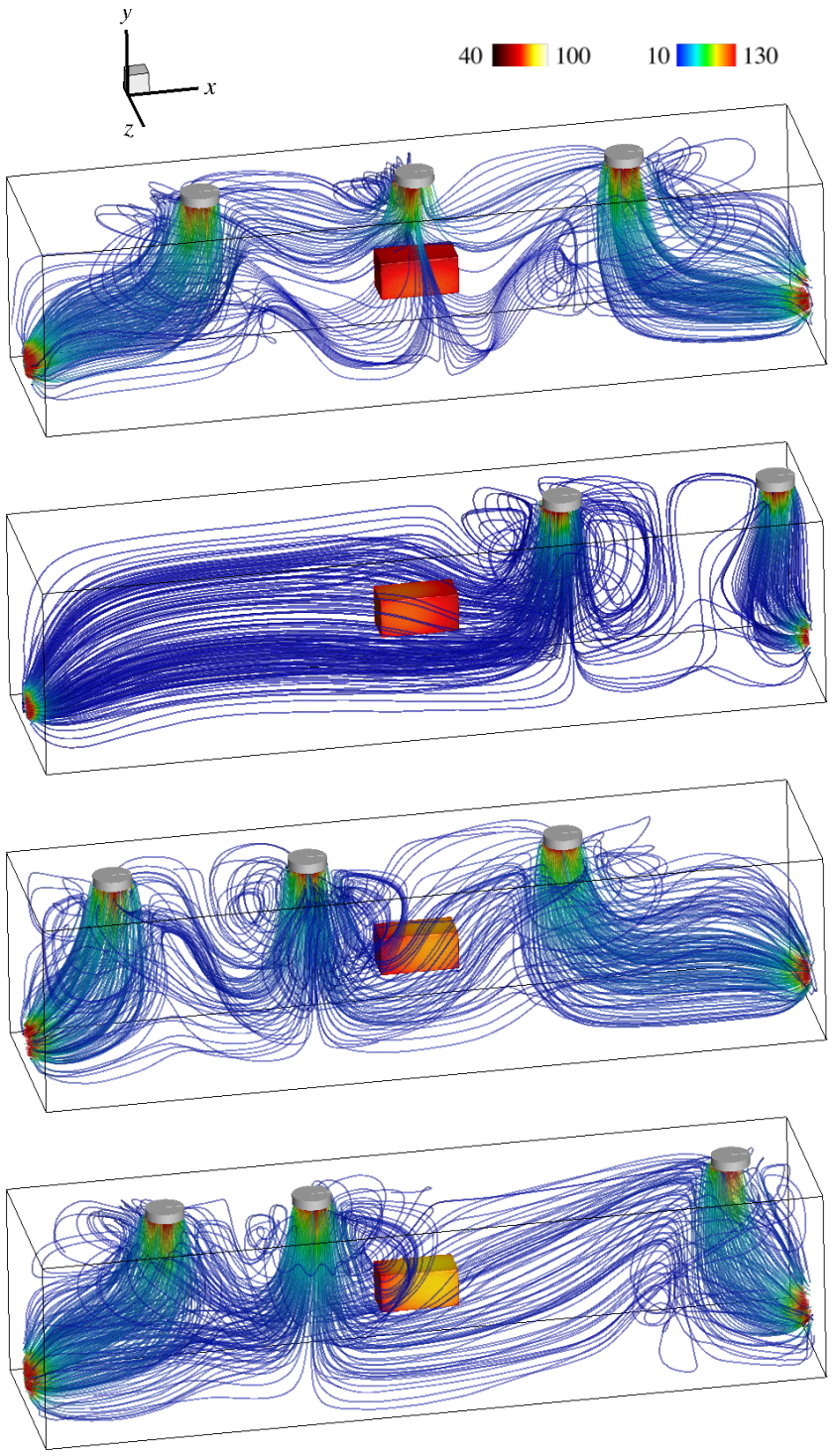

Figure 26: Representative steady-state temperature distributions at the solid/fluid interface together with 3-D streamlines colored by the magnitude of velocity.

and the subscripts ik, jk and ijk denote quantities evaluated at $(x, z) = (i\Delta x, k\Delta z)$, $(y, z) = (j\Delta y, k\Delta z)$ and $(x, y, z) = (i\Delta x, j\Delta y, k\Delta z)$, respectively.

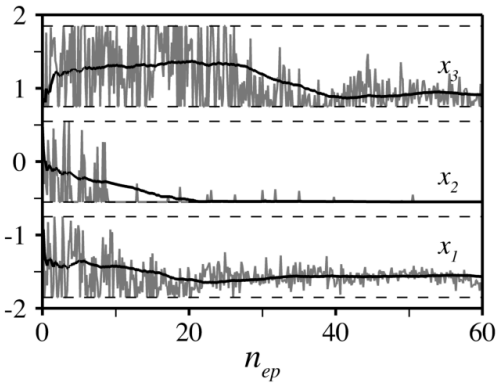

Figure 27: Evolution per learning episode of the instant (in grey) and moving average (in black) injectors center positions under the three-dimensional fixed domain decomposition strategy S_1, with admissible values delimited by the dashed lines.

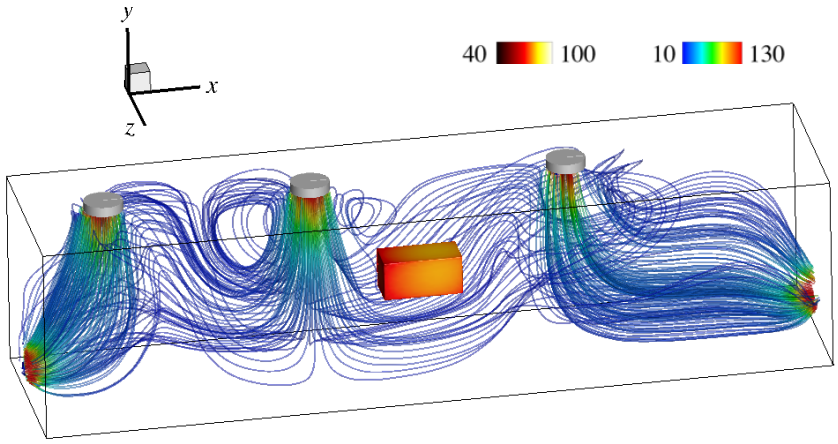

Figure 28: Optimal 3 injector arrangement under the three-dimensional fixed decomposition domain strategy S_1.

All results reported in the following are for $n_j = 3$ injectors. The edge values needed to map the network action output into the actual injectors positions deduce straightforwardly from (40)-(43) substituting the diameter d_i of the 3-D injectors for the length e_i of the 2-D injectors. The same DRL agent is used, that consists of two hidden layers, each holding 2 neurons, and the resolution process uses 8 environments and 2 steps mini-batches to update the network for 32 epochs. Each environment performs 1250 iterations with time step $\Delta t = 0.1$ to march the same initial condition (consisting of zero velocity and uniform temperature, except in the solid domain) to steady state, using the level set, velocity and temperature as multiple-component criterion to adapt the mesh (initially pre-adapted using the sole level set) every 10 time steps under the constraint of a fixed number of elements $n_{el} = 120000$. This is likely insufficient to claim true numerical accuracy, but given the numerical cost (320 3-D simulations per strategy, each of which is performed on 8 cores and lasts 2h30, hence 800h of total CPU cost), we believe this is a reasonable compromise to assess feasibility while producing qualitative results to build on.

6.3 Results

Only the fixed domain decomposition S_1 strategy (in which the top cavity wall is split into n_j equal subdomains and each injector is forced to sit in a different subdomain) and the free S_3 strategy (in which the injectors are entirely independent and free to move along the top cavity wall) are considered here to save computational resources, as learning has been seen to be slower in 2-D under the follow-up S_2 strategy.

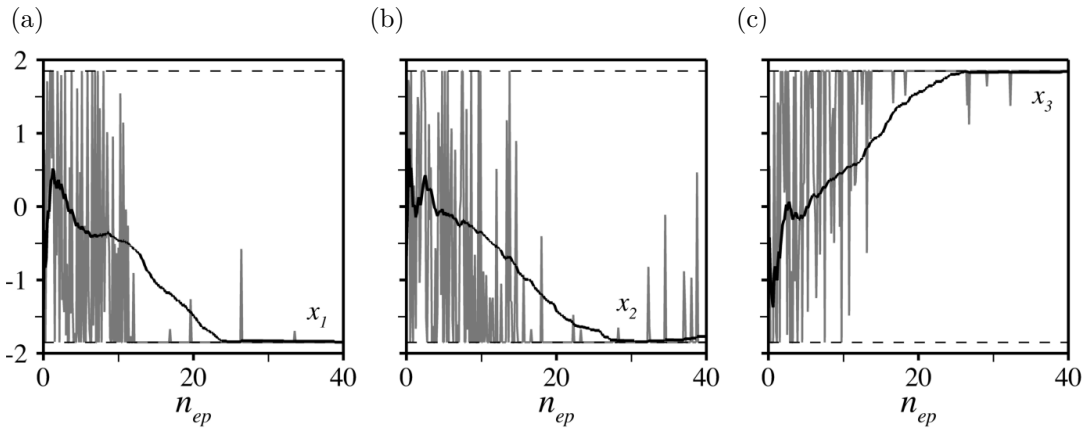

Figure 29: Evolution per learning episode of the instant (in grey) and moving average (in black) injectors center positions under the three-dimensional free strategy S_3, with admissible values delimited by the dashed lines.

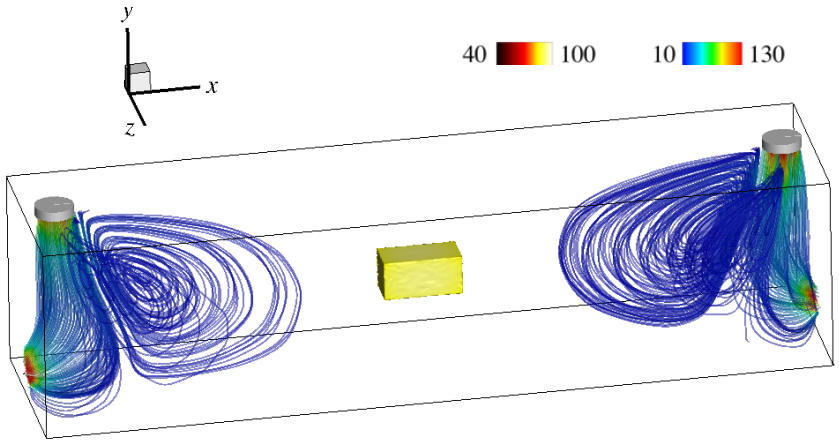

Figure 30: Optimal 3 injector arrangement under the three-dimensional free strategy S_3.

A total of 60 episodes have been run under the fixed domain decomposition strategy S_1. Several representative flow patterns computed over the course of optimization are shown in figure 26 via iso-contours of the steady-state temperature at the fluid-solid interface and 3-D streamlines colored by the magnitude of velocity, to put special emphasis on transverse inhomogeneities and display the increased degree of complexity due to the formation of large-scale horseshoe vortices wrapped around the nozzle jets. We show in figure 27 that the distribution slowly converges to an optimal arrangement consisting of one injector at the left end of the left subdomain ($x_{1\text{opt}} = -1.63$), another one at the left end of the center subdomain ($x_{2\text{opt}} = -0.55$), and a third one at the left end of the right subdomain ($x_{3\text{opt}} = 0.87$), as has been determined by averaging the instant positions of each injector over the latest 10 learning episodes, with variations by roughly ± 0.04 computed from the root-mean-square of the moving average over the same interval. This is larger by one order of magnitude than the variations reported in 2-D, as the agent keeps exploring slightly sub-optimal positions of the lateral injectors, which likely simply reflects the challenging nature of performing three-dimensional optimal control. The 3-D S_1 optimal somehow resemble its 2-D counterpart, namly the center injector is at the exact same position, while the lateral injectors (especially the leftmost one) have been pushed towards the cavity sidewalls. The associated flow pattern is reported in figure 28. The associated optimal reward computed over the same interval is $\langle ||\nabla_{\parallel} T|| \rangle_{\text{opt}} \sim 19.5$, i.e. twice as large than in 2-D, although it is difficult to compare further because of the difference in the Reynolds and Prandtl number.

Another 40 episodes have been run under the free strategy S_3, for which the results are almost identical to their 2-D counterparts, as the distribution converges in figure 29 to an optimal arrangement consisting of two overlapping injectors at the left end of the cavity ($x_{1\text{opt}} = -1.83$ and $x_{2\text{opt}} = -1.82$), and a third injector

	n_j	n_{ep}	x_0	x_1	x_2	x_3	$\langle\|\|\nabla_\parallel T\|\|\rangle$
S_1	3	60	0	-1.63	-0.55	0.87	19.5
S_3	3	40	0	-1.83	-1.82	1.83	4.7

Table 5: Numerical data for the optimal arrangements computed in three-dimensions under strategies S_1 and S_3. All values computed by averaging the instant signal over the 10 latest learning episodes.

at the right end ($x_{3\text{opt}} = 1.83$), with variations by with ± 0.01 for the lateral injectors, but ± 0.03 for the center injector, for which the agent keeps occasionally exploring sub-optimal positions. The corresponding flow pattern shown in figure 30 is thus again symmetrical with two large, 3-D recirculations on either side of the workpiece. The associated optimal reward computed over the same interval is $\langle\|\nabla_\parallel T\|\rangle_{\text{opt}} \sim 4.7$ substantially smaller than that achieved under the 3-D S_1 strategy, which again demonstrates the feasibility to improve performances by allowing overlaps. All relevant numerical data are reported in table 5 for the sake of completeness.

7 Conclusion

This research assesses the ability of deep reinforcement learning (DRL) to guide the optimization and control of conjugate heat transfer systems. It combines a novel, "degenerate" version of the proximal policy optimization (PPO) algorithm, that trains a neural network in optimizing the system only once per learning episode, and an in-house stabilized finite elements environment combining variational multiscale (VMS) modeling of the governing equations, immerse volume method, and multi-component anisotropic mesh adaptation, that computes the numerical reward fed to the neural network. The approach is shown capable of optimizing two- and three dimensional systems exhibiting natural and forced convection dominated heat transfer. It is especially applied to identify optimal distribution of injectors and optimal position of a hot workpiece to reduce inhomogeneous impingement cooling under various control strategies.

Fluid dynamicists have just begun to gauge the relevance of deep reinforcement learning techniques to assist the design of optimal control strategies. This research weighs in on this issue and adds values to the shallow literature on this subject by showing that the proposed single-step PPO holds a high potential as a reliable, go-to black-box optimizer for complex conjugate heat transfer problems. Future research in this field should aim at consolidating the acquired knowledge, at improving the computational efficiency (by a fine-tuning of the hyper parameters, or using pre-trained deep learning models) and at boosting the convergence capabilities (via coupling with a surrogate model trained on-the-fly, or using non-normal probability density functions, or modifying the balance between exploration and exploitation, as the PPO loss is specifically built to avoid a performance collapse by preventing large updates of the policy). The design of relevant numerical rewards under partial state information is another issue that deserves consideration.

Scope is another key ingredient to pushing forward the state of the art. A short-term objective would be to quickly tackle more complex test cases exhibiting time-dependent dynamics and turbulence, which the numerical framework is perfectly suited to do via a combination of Reynolds-averaged Navier–Stokes modeling [63, 64] and second-order, semi-implicit time discretization [65]. We believe that this will highlight even more clearly the relevance of the methodology, as it is speculated in [30] that DRL should be able to handle chaotic systems without suffering from the shortcomings and limitations of the adjoint method, and [27] consistently report that DRL outperforms a canonical linear proportional-derivative controller in controlling turbulent natural convection. The long-term objective would be to enrich the description of the test cases using multi-physics modeling (e.g., radiative heat transfer, phase transformation), to pave the way toward flexible, ready-to-use control of industrially relevant applications, such as thermal comfort for building design or manufacturing processes.

Acknowledgements

This work is supported by the Carnot M.I.N.E.S. Institute through the M.I.N.D.S. project.

References

[1] A. Jameson. Aerodynamic design via control theory. J. Sci. Comput., 3:233–260, 1998.

[2] M. D. Gunzburger. Perspectives in flow control and optimization. SIAM, Philadelphia, 2002.

[3] T.R. Bewley. Flow control : new challenges for a new renaissance. Prog. Aerosp. Sci., 37:21–58, 2001.

[4] K. Momose, K. Abe, and H. Kimoto. Reverse computation of forced convection heat transfer for optimal control of thermal boundary conditions. Heat Tran. Asian Res., 33:161–174, 2004.

[5] A. Belmiloudi. Robin-type boundary control problems for the nonlinear Boussinesq type equations. J. Math. Anal. Appl., 273:428–456, 2002.

[6] G. Bärwolff and M. Hinze. Optimization of semiconductor melts. Z. Angew. Math. Mech., 86:423–437, 2006.

[7] J.L. Boldrini, E. Fernàndez-Cara, and M.A. Rojas-Medar. An optimal control problem for a generalized Boussinesq model: The time dependent case. Rev. Mat. Comput., 20:339–366, 2007.

[8] H. Karkaba, T. Dbouk, C. Habchi, S. Russeil, T. Lemenand, and D. Bougeard. Multi objective optimization of vortex generators for heat transfer enhancement using large design space exploration. Chem. Eng. Process., 2020 (accepted).

[9] P. Meliga and J.-M. Chomaz. Global modes in a confined impinging jet: application to heat transfer and control. Theor. Comput. Fluid Dyn., 25(1):179–193, 2011.

[10] D.E. Rumelhart, G.E. Hinton, and R.J. Williams. Learning representations by back-propagating errors. Nature, 323:533–536, 1986.

[11] J. Kober, J. A. Bagnell, and J. Peters. Reinforcement learning in robotics: A survey. The International Journal of Robotics Research, 32(11):1238–1274, 2013.

[12] V. Mnih, K. Kavukcuoglu, D. Silver, Rusu. A.A., Veness J., M.G. Bellemare, A. Graves, M. Riedmiller, A. K. Fidjeland, G. Ostrovski, S. Petersen, C. Beattie, A. Sadik, I. Antonoglou, H. King, D. Kumaran, D. Wierstra, S. Legg, and D. Hassabis. Human-level control through deep reinforcement learning. Nature, 518:7540, 2015.

[13] Geoffrey E Hinton, Alex Krizhevsky, and Ilya Sutskever. Imagenet classification with deep convolutional neural networks. Advances in neural information processing systems, 25:1106–1114, 2012.

[14] B. Lusch, J. N. Kutz, and S. L Brunton. Deep learning for universal linear embeddings of nonlinear dynamics. Nature communications, 9(1):1–10, 2018.

[15] M. Raissi, A. Yazdani, and G. E. Karniadakis. Hidden Fluid Mechanics: A Navier-Stokes Informed Deep Learning Framework for Assimilating Flow Visualization Data. arXiv, 2018.

[16] A. D. Beck, D. G. Flad, and C.-D. Munz. Deep Neural Networks for Data-Driven Turbulence Models. arXiv, 2018.

[17] S. L. Brunton, B.R. Noack, and P. Koumoutsakos. Machine learning for fluid mechanics. Annu. Rev. Fluid Mech., 52:477–508, 2020.

[18] D. Silver, J. Schrittwieser, K. Simonyan, I. Antonoglou, A. Huang, A. Guez, T. Hubert, L. Baker, M. Lai, A. Bolton, Y. Chen, T. Lillicrap, F. Hui, L. Sifre, G. van den Driessche, T. Graepel, and D. Hassabis. Mastering the game of go without human knowledge. Nature, 550(7676):354–359, 2017.

[19] J. Hwangbo, J. Lee, A. Dosovitskiy, D. Bellicoso, V. Tsounis, V. Koltun, and M. Hutter. Learning agile and dynamic motor skills for legged robots. Science Robotics, 4(26):eaau5872, 2019.

[20] A.V. Bernstein and E.V. Burnaev. Reinforcement learning in computer vision. Proc. SPIE 10696, 10th International Conference on Machine Vision (ICMV 2017), 2018.

[21] T. P. Lillicrap, J. J. Hunt, A. Pritzel, N. Heess, T. Erez, Y. Tassa, D. Silver, and D. Wierstra. Continuous control with deep reinforcement learning. arXiv e-prints, 2015.

[22] J. Schulman, F. Wolski, P. Dhariwal, A. Radford, and O. Klimov. Proximal Policy Optimization Algorithms. arXiv e-prints, July 2017.

[23] P. Ma, Y. Tian, Z. Pan, B. Ren, and D. Manocha. Fluid directed rigid body control using deep reinforcement learning. ACM Transactions on Graphics (TOG), 37(4):1–11, 2018.

[24] J. Rabault, M. Kuchta, A. Jensen, U. Réglade, and N. Cerardi. Artificial neural networks trained through deep reinforcement learning discover control strategies for active flow control. Journal of Fluid Mechanics, 865:281–302, 2019.

[25] H. Tang, J. Rabault, A. Kuhnle, Y. Wang, and T. Wang. Robust active flow control over a range of Reynolds numbers using an artificial neural network trained through deep reinforcement learning. Phys. Fluids, 32:053605, 2020.

[26] J. Viquerat, J. Rabault, A. Kuhnle, H. Ghraieb, and E. Hachem. Direct shape optimization through deep reinforcement learning. arXiv preprint arXiv:1908.09885, 2019.

[27] G. Beintema, A. Corbetta, L. Biferale, and F. Toschi. Controlling Rayleigh-B\'enard convection via reinforcement learning. arXiv preprint arXiv:2003.14358, 2020.

[28] H. Kazmi, F. Mehmood, S. Lodeweyckx, and J. Driesen. Gigawatt-hour scale savings on a budget of zero: Deep reinforcement learning based optimal control of hot water systems. Energy, 144:159–168, 2018.

[29] T. Zhang, J. Luo, P. Chen, and J. Liu. Flow rate control in smart district heating systems using deep reinforcement learning. arXiv preprint arXiv:1912.05313, 2019.

[30] H. Ghraieb, P. Meliga, J. Viquerat, and E. Hachem. Optimization and passive flow control using single-step deep reinforcement learning. Phys. Rev. Fluids (submitted), 2020.

[31] C. Gruau and T. Coupez. 3d tetrahedral, unstructured and anisotropic mesh generation with adaptation to natural and multidomain metric. Comput. Methods Appl. Mech. Engrg., 194:4951–4976, 2005.

[32] M. Bernacki, Y. Chastel, T. Coupez, and R.E. Logé. Level set framework for the numerical modelling of primary recrystallization in polycrystalline materials. Scr. Mater., 58:1129–1132, 2008.

[33] Y. Mesri, H. Digonnet, and T. Coupez. Advanced parallel computing in material forming with CIMLib. Eur. J. Comput. Mech., 18:669–694, 2009.

[34] T. Coupez. Metric construction by length distribution tensor and edge based error for anisotropic adaptive meshing. J. Comput. Phys., 230:2391–2405, 2011.

[35] S.V. Patankar. Numerical heat transfer and fluid flow. Taylor and Francis, 1980.

[36] T. J. R. Hughes, G. R. Feijóo, L. Mazzei, and J.-B. Quincy. The variational multiscale method - a paradigm for computational mechanics. Comput. Methods Appl. Mech. Engrg., 166:3–24, 1998.

[37] R. Codina. Stabilization of incompressibility and convection through orthogonal sub-scales in finite element methods. Comput. Methods Appl. Mech. Engrg., 190:1579–1599, 2000.

[38] Y. Bazilevs, V. M. Calo, J. A. Cottrell, T. J. R. Hughes, A. Reali, and G. Scovazzi. Variational multiscale residual-based turbulence modeling for large eddy simulation of incompressible flows. Comput. Methods Appl. Mech. Engrg., 197:173–201, 2007.

[39] E. Hachem, B. Rivaux, T. Kloczko, H. Digonnet, and T. Coupez. Stabilized finite element method for incompressible flows with high Reynolds number. J. Comput. Phys., 229(23):8643–8665, 2010.

[40] E. Hachem, T. Kloczko, H. Digonnet, and T. Coupez. Stabilized finite element solution to handle complex heat and fluid flows in industrial furnaces using the immersed volume method. Int. J. Numer. Methods Fluids, 68:99–121, 2012.

[41] R. Codina. Stabilized finite element approximation of transient incompressible flows using orthogonal subscales. Comput. Methods Appl. Mech. Engrg., 191:4295–4321, 2002.

[42] E. Hachem, S. Feghali, R. Codina, and T. Coupez. Immersed stress method for fluid-structure interaction using anisotropic mesh adaptation. Int. J. Numer. Meth. Eng., 94:805–825, 2013.

[43] R. Codina. Comparison of some finite element methods for solving the diffusion-convection-reaction equation. Comput. Methods Appl. Mech. Engrg., 156:185–210, 1998.

[44] S. Badia and R. Codina. Analysis of a stabilized finite element approximation of the transient convection-diffusion equation using an ALE framework. SIAM Journal on Numerical Analysis, 44:2159–2197, 2006.

[45] A. N. Brooks and T.J.R. Hughes. Streamline upwind/Petrov-Galerkin formulations for convection dominated flows with particular emphasis on the incompressible Navier-Stokes equations. Comput. Methods Appl. Mech. Engrg., 32:199–259, 1982.

[46] A.C. Galeão and E.G.D. Do Carmo. A consistent approximate upwind Petrov-Galerkin method for convection-dominated problems. Comput. Methods Appl. Mech. Engrg., 68:83–95, 1988.

[47] E. Hachem, H. Digonnet, E. Massoni, and T. Coupez. Immersed volume method for solving natural convection, conduction and radiation of a hat-shaped disk inside a 3d enclosure. International Journal of numerical methods for heat & fluid flow, 2012.

[48] E. Hachem, G. Jannoun, J. Veysset, M. Henri, R. Pierrot, I. Poitrault, E. Massoni, and T. Coupez. Modeling of heat transfer and turbulent flows inside industrial furnaces. Simul. Model. Pract. Th., 30:35–53, 2013.

[49] I. Goodfellow, Y. Bengio, and A. Courville. The Deep Learning Book. MIT Press, 2017.

[50] Richard S Sutton and Andrew G Barto. Reinforcement learning: An introduction. MIT press, 2018.

[51] A. Kakade. A natural policy gradient. Adv. Neural Inf. Process Syst., 14:1531–1538, 2001.

[52] John Schulman, Sergey Levine, Philipp Moritz, Michael I. Jordan, and Pieter Abbeel. Trust Region Policy Optimization. arXiv e-prints, February 2015.

[53] Y. Wang, H. He, X. Tan, and Y. Gan. Trust region-guided proximal policy optimization. arXiv preprint arXiv:1901.10314, 2019.

[54] A. Hill, A. Raffin, M. Ernestus, A. Gleave, A. Kanervisto, R. Traore, P. Dhariwal, C. Hesse, O. Klimov, A. Nichol, M. Plappert, A. Radford, J. Schulman, S. Sidor, and Y. Wu. Stable baselines. https://github.com/hill-a/stable-baselines, 2018.

[55] G. Brockman, V. Cheung, L. Pettersson, J. Schneider, J. Schulman, J. Tang, and W. Zaremba. Openai gym, 2016.

[56] G. de Vahl Davis and I.P. Jones. Natural convection in a square cavity: a comparison exercise. Int. J. Numer. Methods Fluids, 3:227–248, 1983.

[57] H.N. Dixit and V. Babu. Simulation of high Rayleigh number natural convection in a square cavity using the lattice Boltzmann method. Int. J. Heat Mass Transfer, 49:727–739, 2006.

[58] N.C. Markatos and K.A. Pericleous. Laminar and turbulent natural convection in an enclosed cavity. Int. J. Heat Mass Transfer, 27:772–775, 1984.

[59] G. Barakos and E. Mitsoulis. Natural convection flow in a square cavity revisited: laminar and turbulent models with wall functions. Int. J. Numer. Methods Fluids, 18:695–719, 1994.

[60] K. Khanafer, K. Vafai, and M. Lightstone. Buoyancy-driven heat transfer enhancement in a two-dimensional enclosure utilizing nanofluids. Int. J. Heat Mass Transfer, 46:3639–3653, 2003.

[61] A. Lazaric, M. Restelli, and A. Bonarini. Reinforcement learning in continuous action spaces through sequential Monte Carlo methods. In Procs. of the 35th International Conference on Machine Learning, pages 4587–4596, 2018.

[62] K. Lee, S.A. Kim, and J. Choi. Deep reinforcement learning in continuous action spaces: a case study in the game of simulated curling. In Procs. of the 35th International Conference on Machine Learning, pages 4587–4596, 2018.

[63] J. Sari, F. Cremonesi, M. Khalloufi, F. Cauneau, P. Meliga, Y. Mesri, and E. Hachem. Anisotropic adaptive stabilized finite element solver for rans models. Int. J. Numer. Methods Fluids, 86:717–736, 2018.

[64] G. Guiza, A. Larcher, A. Goetz, L. Billon, P. Meliga, and E. Hachem. Anisotropic boundary layer mesh generation for reliable 3D unsteady RANS simulations. Finite Elem. Anal. Des., 170:103345, 2020.

[65] P. Meliga and E. Hachem. Time-accurate calculation and bifurcation analysis of the incompressible flow over a square cavity using variational multiscale modeling. J. Comput. Phys., 376:952–972, 2019.